

# Monthly Weather Review

## Microscale Updrafts Within the U.S. Northeast Coastal Snowstorms Using High-Resolution Cloud Radar Measurements

--Manuscript Draft--

<b>Manuscript Number:</b>	
<b>Full Title:</b>	Microscale Updrafts Within the U.S. Northeast Coastal Snowstorms Using High-Resolution Cloud Radar Measurements
<b>Article Type:</b>	Article
<b>Corresponding Author:</b>	Mariko Oue Stony Brook University Stony Brook , New York UNITED STATES
<b>Corresponding Author's Institution:</b>	Stony Brook University
<b>First Author:</b>	Mariko Oue
<b>Order of Authors:</b>	Mariko Oue Brian A. Colle Sandra E. Yuter Pavlos Kollias Phillip Yeh Laura M. Tomkins
<b>Abstract:</b>	Limited knowledge exists about ~100 m scale precipitation processes within U.S. Northeast coastal snowstorms because of a lack of high-resolution observations. We investigate characteristics of microscale updraft regions within the cyclone comma head and their relationships with snowbands, wind shear, frontogenesis, and vertical mass flux using high-spatiotemporal resolution vertically-pointing Ka-band radar measurements, soundings, and reanalysis data for four snowstorms observed at Stony Brook, NY. Updraft regions are defined as contiguous time-height plotted areas with upward Doppler velocity without hydrometeor sedimentation that is equal to or greater than 0.4 m s <sup>-1</sup> . Most updraft regions in the time-height data occur on a time scale of seconds (< 20 sec), which is equivalent to spatial scales < 500 m. These small updraft regions within cloud echo occur more than 30% of the time for three of the four cases and 18% for the other case. They are found at all altitudes and can occur with or without frontogenesis and with or without snowbands. The updraft regions with relatively large Doppler spectrum width (> 0.4 m s <sup>-1</sup> ) occur more frequently within midlevels of the storms, where there is a moist shear instability layer. The updraft regions produced higher mass flux when they are closer together in space and time. The higher values of vertically-integrated upward mass flux within updraft regions often occur during snowbands with background ascent from frontogenesis.
<b>Suggested Reviewers:</b>	Lynn McMurdie University of Washington lynnm@uw.edu  David Plummer University of Illinois Urbana-Champaign dplumme1@uwoyo.edu  David Novak National Weather Service Eastern Region david.novak@noaa.gov

1     **Microscale Updrafts Within the U.S. Northeast Coastal Snowstorms Using**  
2             **High-Resolution Cloud Radar Measurements**

3  
4     Mariko Oue<sup>1</sup>, Brian A. Colle<sup>1</sup>, Sandra E. Yuter<sup>2</sup>, Pavlos Kollias<sup>1,3</sup>, Phillip Yeh<sup>1</sup>, Laura M.  
5             Tomkins<sup>2</sup>,

6             1. *Stony Brook University, Stony Brook, NY*

7             2. *North Carolina State University*

8             3. *Brookhaven National Laboratory*

9  
10             Submitted to Monthly Weather Review

11             13 March 2023

12  
13             *Corresponding author: Mariko Oue, mariko.oue@stonybrook.edu*

14 **ABSTRACT**

15 Limited knowledge exists about ~100 m scale precipitation processes within U.S. Northeast  
16 coastal snowstorms because of a lack of high-resolution observations. We investigate  
17 characteristics of microscale updraft regions within the cyclone comma head and their  
18 relationships with snowbands, wind shear, frontogenesis, and vertical mass flux using high-  
19 spatiotemporal resolution vertically-pointing Ka-band radar measurements, soundings, and  
20 reanalysis data for four snowstorms observed at Stony Brook, NY. Updraft regions are defined as  
21 contiguous time-height plotted areas with upward Doppler velocity without hydrometeor  
22 sedimentation that is equal to or greater than  $0.4 \text{ m s}^{-1}$ . Most updraft regions in the time-height  
23 data occur on a time scale of seconds ( $< 20 \text{ sec}$ ), which is equivalent to spatial scales  $< 500 \text{ m}$ .  
24 These small updraft regions within cloud echo occur more than 30% of the time for three of the  
25 four cases and 18% for the other case. They are found at all altitudes and can occur with or without  
26 frontogenesis and with or without snowbands. The updraft regions with relatively large Doppler  
27 spectrum width ( $> 0.4 \text{ m s}^{-1}$ ) occur more frequently within midlevels of the storms, where there is  
28 a moist shear instability layer. The updraft regions produced higher mass flux when they are closer  
29 together in space and time. The higher values of vertically-integrated upward mass flux within  
30 updraft regions often occur during snowbands with background ascent from frontogenesis.

31  
32  
33 **SIGNIFICANCE STATEMENT**

34 Small-scale ( $< 500 \text{ m}$ ) upward motions within four snowstorms along the U.S. Northeast Coast are  
35 analyzed for the first time using high spatiotemporal resolution millimeter-wavelength cloud radar  
36 pointed vertically. The analysis reveals these updrafts appear in the storms regardless of whether  
37 snowbands are present or whether there is forcing for ascent. The more turbulent and stronger  
38 updrafts frequently occur in midlevels of storms and contribute to upward mass flux when they  
39 are closer together in space and time with instability from vertical shear during snowband periods.

## 41 **1. Introduction**

42

43 Snowbands in the comma head of winter storms are responsible for much of the heavy snowfall  
44 over the northeast United States. Because of the large societal impacts of these winter storms, they  
45 have been studied for decades using both numerical models and observations (e.g., Novak et al.  
46 2008; Stark et al. 2013; Plummer et al. 2014; McMurdie et al. 2022). These studies have shown a  
47 spectrum of snowbands, ranging from primary bands, which are defined as a single reflectivity  
48 feature  $> 250$  km in length, 20–100 km in width, and with intensities of  $>30$  dBZ maintained for  
49 at least 2 hours, to smaller-scale multi-bands which occur in groups (Ganetis et al. 2018). The  
50 mechanisms that result in the variations in snowband characteristics are not well known.

51 Previous studies on snowband formation have focused on the mesoscale ingredients of lift  
52 along a mid-level trough, instability, and moisture (Novak et al. 2010). Primary bands are often  
53 associated with mid-level frontogenesis (e.g., Novak et al. 2004, 2008), as well as a spectrum of  
54 instabilities, such as conditional symmetric instability (e.g., Schultz and Schumacher 1999),  
55 conditional instability (e.g., Trapp et al. 2001; Morales 2008) and inertial instability (e.g., Jurewicz  
56 and Evans 2004; Schultz and Knox 2007). Earlier modeling and theoretical studies of multi-bands  
57 focused on the superposition of a frontogenetical circulation and either CI or CSI instabilities (Xu  
58 1992). However, Ganetis et al. (2018) showed that these bands often develop in a region of little  
59 or no frontogenesis; thus, other mechanisms may be responsible, such as elevated convection,  
60 generating cells, shear instabilities, and gravity wave activity, which often occur at smaller scales  
61 than frontogenesis (Bosart and Sanders 1986; Zhang et al. 2001, 2003; Kumjian et al. 2014;  
62 Plummer et al. 2014, 2015; Rauber et al. 2014, 2017; Rosenow et al. 2014, 2018; Keeler et al.  
63 2016a, b, 2017; Lackmann and Thompson 2019; McMurdie et al. 2022).

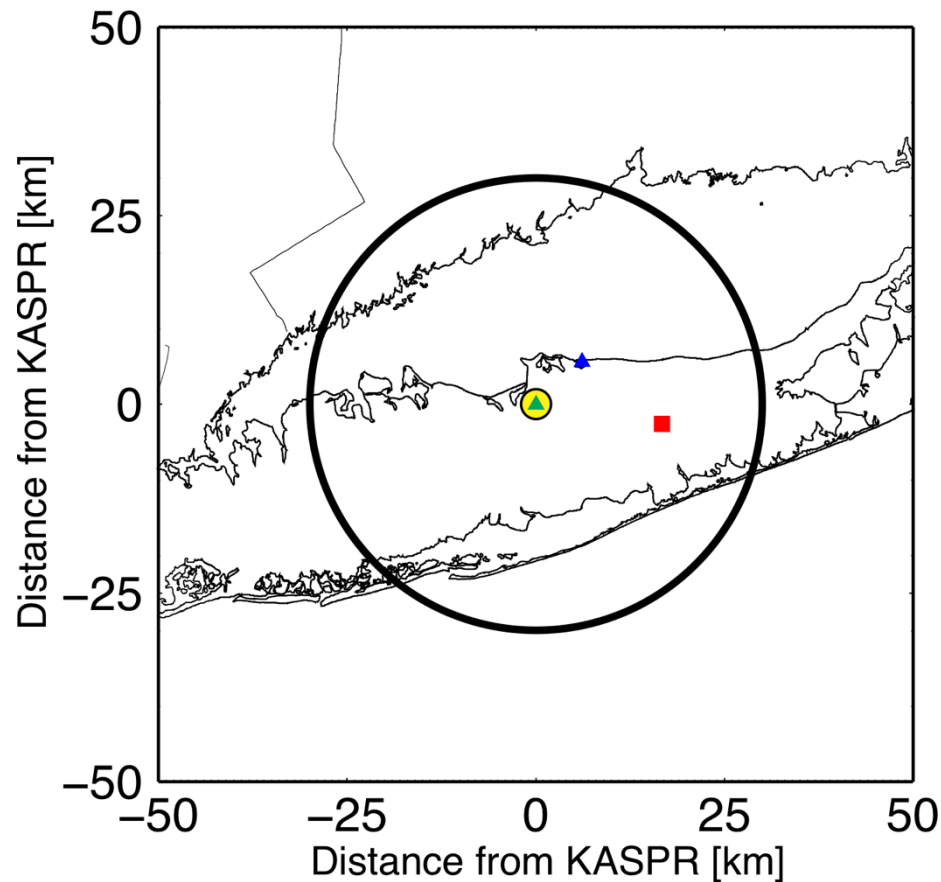
64 Snowbands also have variable microphysics that can impact precipitation rates. Studies using  
65 in-situ surface measurements observed a variety of snowflake habits and degrees of riming within  
66 the cyclone comma head and storm evolution (e.g., Stark et al. 2013; Colle et al., 2014). In  
67 particular, the microphysical processes can change across the snowband from more rimed on the  
68 east (warmer) side to more dry snow on the west (colder) side. Those microphysical studies using  
69 in-situ surface measurements have also revealed that upper-level cloud structures, dynamics, and  
70 microphysics (i.e., generating cells, turbulence) strongly impact the surface precipitation, while  
71 internal cloud processes can interact with each other producing complex microphysics. Field

72 campaigns using high spatiotemporal resolution airborne radars (e.g., ProfiLing Of Winter Storms  
73 [PLOWS], e.g. Rauber et al. 2014) revealed microscale convective updrafts producing generating  
74 cells which contributed to greater ice production by diffusion, riming, and aggregation processes  
75 (Plummer et al. 2014). Kumjian and Lombardo (2017) utilized the dual-polarization capabilities  
76 from the WSR-88D network to find planar crystal growth and precipitation-type transitions  
77 (snow/rain/ice) and noted that the Rapid Refresh model reanalysis (50 vertical levels and 13-km  
78 horizontal grid space) failed to capture the complex microphysical evolution. Numerical  
79 simulation studies have shown deficiencies in many of the bulk microphysical schemes for winter  
80 storms (e.g., Naeger et al. 2017;2020; Molthan et al. 2016).

81 Since microphysical processes are strongly related to small-scale air motions, the impacts of  
82 small-scale dynamical characteristics, which are usually not resolved by either the regional models  
83 or operational radars, need to be explored to explain the large variability of microphysical  
84 characteristics. To fill this gap, we need detailed, high-spatiotemporal resolution observations of  
85 snowstorms over the northeast U.S. The recent, ongoing field campaign, the Investigation of  
86 Microphysics and Precipitation of Atlantic Coast-Threatening Snowstorms (IMPACTS,  
87 McMurdie et al. 2022) focuses on improving the understanding of snowfall processes, remote  
88 sensing of snow, and the prediction of banded structure and evolution using multi-scale  
89 observations including in-situ and vertically-pointing and scanning remote sensing measurements  
90 from both airborne and ground-based platforms.

91 The Ka-band Scanning Polarimetric Radar (KASPR) is an ideal remote sensing instrument to  
92 study the fine scale kinematic and microphysical characteristics of winter storms (e.g. Oue et al.  
93 2017; Kollias et al. 2020). KASPR has been part of the Stony Brook University and Brookhaven  
94 National Laboratory Radar Observatory (SBRO) since 2017 and installed in the Stony Brook  
95 University site (Fig. 1). KASPR polarimetric and Doppler capabilities have revealed fine scale  
96 dynamical and microphysical features within winter storms (Kumjian et al. 2020; Lamer et al.  
97 2021; Oue et al. 2021). This study uses data from four winter storms and focuses on characteristics  
98 of microscale ( $< 1$  km) updraft regions, their relationship with ambient conditions, and their role  
99 in vertical mass transport. Section 2 describes the datasets used in this study. Section 3 summarizes  
100 the meteorological context and evolution of the four events and the corresponding KASPR  
101 observations. The relationships among the observed updraft structures, precipitation features, and  
102 other storm parameters important for forcing for ascent (e.g., frontogenesis, Petterssen, 1956) and

103 wind shear are discussed in section 4. Finally, summary and conclusions are presented in Section  
104 5.  
105



106  
107  
108 Figure 1: Locations of KASPR (the center of this display, yellow dot), the nearest NWS sounding site  
109 (OKX, red square), and two SBU mobile sounding sites (Stony Brook by green triangle (same as the  
110 KASPR location) and Cedar Beach by blue triangle). A large circle represents the KASPR's 30-km radius  
111 maximum observation range by PPI.  
112

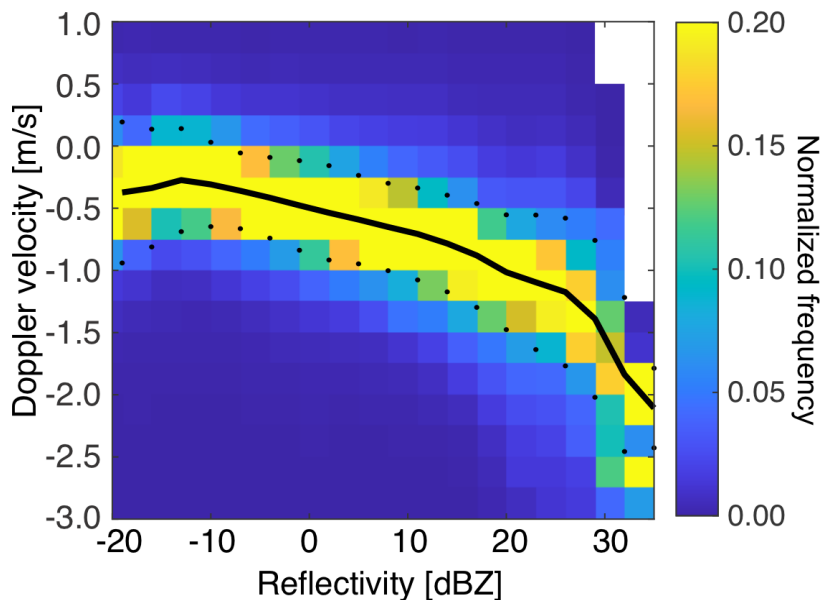
## 113 2. Data and Methods

### 114 a. *Ka-band Scanning Polarimetric Radar (KASPR)*

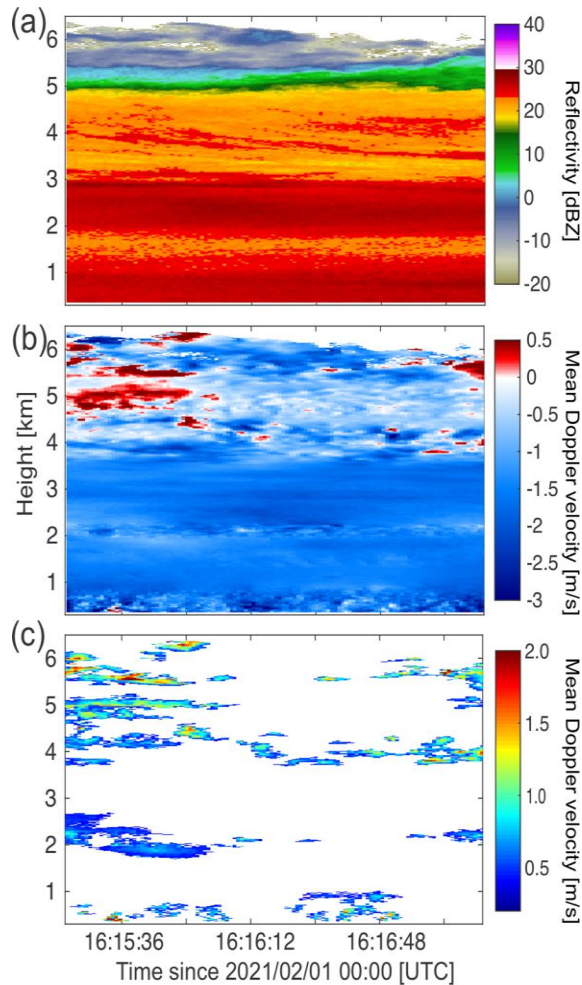
115 KASPR is a state-of-the-art 35-GHz cloud scanning radar with a beamwidth of  $0.32^\circ$ , capable  
116  
117 of collecting reflectivity, Doppler velocity, Doppler spectrum width, and the standard set of  
118 polarimetric radar variables. The KASPR power measurements are calibrated using a corner  
119 reflector technique and the polarimetric measurements are calibrated using natural targets. The  
120 detailed specification of KASPR is available in Kumjian et al. (2020) and Kollias et al. (2020).  
121

122 This study does not apply attenuation corrections for hydrometeor condensate and carefully selects  
123 periods of snow through the columns to avoid significant attenuation by liquid precipitation.

124 To observe the microphysical and dynamical characteristics of snowstorms while maximizing  
125 the KASPR polarimetric and Doppler spectrum capabilities, KASPR executed a scanning strategy  
126 that consisted of a Plan Position Indicator (PPI) surveillance scan at 15° elevation angle (and 20°  
127 for the 2018 winter), a zenith pointing (90° elevation angle) PPI for calibration, horizon-to-horizon  
128 Range-Height Indicator (RHI, Kollias et al., 2014) scans, and a vertically pointing mode (VPT).  
129 This pattern was repeated and took approximately 13-15 minutes to complete. The PPI and RHI  
130 scans were performed with a full polarimetry mode and scan speeds of 6° s<sup>-1</sup> and 2° s<sup>-1</sup>,  
131 respectively, to collect data with a 30-m range-gate spacing, 0.6° PPI azimuthal spacing and 0.3°  
132 RHI elevation spacing. The VPT mode was executed with only horizontally polarized waves  
133 transmitted and both horizontally and vertically polarized waves received. The KASPR radar was  
134 in VPT mode for consecutive periods lasting 2 to 5 min with a 15-m range-gate spacing. Based on  
135 the beamwidth, the horizontal resolution at a 10 km range is approximately 56 m.



136  
137 Figure 2: Reflectivity versus mean Doppler velocity from all KASPR VPT data used in this study from the  
138 selected four cases. Color shade represents frequency normalized every 3 dBZ. Solid and dotted lines represent  
139 mean Doppler velocity every 3 dBZ and mean Doppler velocity  $\pm$  standard deviation, respectively. Doppler  
140 velocity is scaled for air density using the nearest sounding data.



141  
 142 Figure 3. Height-versus-time cross sections of (a) KASPR reflectivity and (b) mean Doppler velocity from  
 143 vertically-pointing measurements on February 1, 2021 from 16:15:18 to 16:20:10 UTC, (c) the estimated vertical  
 144 air motion  $> 0.4 \text{ m s}^{-1}$  (mean Doppler velocity without hydrometeor sedimentation). Very small updraft regions  
 145  $< 15$  range-bins are not included in the analysis.

146

147 The VPT measurements are used to identify updraft regions (URs) in time-height plots based  
 148 on mean Doppler velocity. First, Doppler velocity with reflectivity  $< -20 \text{ dBZ}$  is removed from the  
 149 analysis since it is too noisy. Then the hydrometeor sedimentation component is removed from the  
 150 measured Doppler velocity following Protat and Williams (2011). The hydrometeor sedimentation  
 151 is estimated as the mean Doppler velocity for every 3 dBZ from  $-20 \text{ dBZ}$  to  $34 \text{ dBZ}$ , assuming that  
 152 the mean vertical air motion for a certain time period at a given height is  $\sim 0 \text{ m s}^{-1}$ . Figure 2 presents  
 153 the Z-V relationship from all VPT data (negative values indicate downward motion) from the four  
 154 selected cases (described in Sect. 3). We estimated the reflectivity versus Doppler-velocity (Z-V)  
 155 relationship every 500 m using hourly VPT data and used the median value of Doppler velocity as  
 156 the hydrometeor sedimentation at each dBZ bin at each height-hour window. For each estimation

157 of Z-V relationship (each height-hour window), when the median Doppler velocity became  
158 positive (upward motion) or the number of samples at each dBZ bin was less than 100, we used  
159 the statistical value of the median Doppler velocity shown in Fig. 2 for it to be considered  
160 sedimentation. To determine if a region is an updraft, the measured Doppler velocity minus the  
161 estimated hydrometeor sedimentation for each reflectivity bin in that range gate has to be positive.  
162 In this study, to avoid accounting for range gates not representing updrafts due to the variability  
163 of the Doppler velocity, we considered updraft regions to be range gates where the measured  
164 Doppler velocity minus the estimated hydrometeor sedimentation was greater than equal to  $0.4 \text{ m s}^{-1}$ .  
165 The threshold of  $0.4 \text{ m s}^{-1}$  is the value of standard deviation of Doppler velocity in Fig. 2. For  
166 example, in Fig. 2, for 0 dBZ the estimated sedimentation speed is  $-0.2 \text{ m s}^{-1}$  so measured Doppler  
167 velocity values  $> 0.2 \text{ m s}^{-1}$  are considered to be updrafts. For 20 dBZ the estimated sedimentation  
168 speed is  $-0.62 \text{ m/s}$  so measured Doppler velocity values  $> -0.02 \text{ m s}^{-1}$  are considered to be updrafts.  
169 We defined the updraft region (UR) as a region with at least 15 updraft range-gates connected in  
170 time or height. Small regions having less than 15 range-bins are removed from the analysis.

171 Figure 3 shows an example of 5-min VPT reflectivity (Fig. 3a), Doppler velocity (Fig. 3b), and  
172 the identified updrafts (negative indicates a downward motion, Fig. 3c) from 16:15:18 UTC for 5  
173 minutes on 1 February 2021. We tested other Doppler velocity thresholds ( $0.0 \text{ m s}^{-1}$  and  $0.6 \text{ m s}^{-1}$ )  
174 and confirmed that varying the threshold within this range had little impact on the results. For  
175 example, when the threshold is increased from  $0.4 \text{ m s}^{-1}$  to  $0.6 \text{ m s}^{-1}$ , the total number of URs  
176 decreases by 28-49%; however, the shapes of the normalized size distribution (discussed in Section  
177 4) and vertical distribution do not change.

178 The duration of the detected URs is defined as the time between the earliest and latest times of  
179 the appearance of the region. The thickness is defined as a height between the lowest and highest  
180 range-bins of the appearance of the region. The altitude of individual updraft regions is estimated  
181 as a mean of altitudes of range gates in the updraft regions (Fig. 3c). Doppler spectrum width (SW)  
182 from the VPT measurements is averaged in each UR (Fig. 2d). We use  $\text{SW} > 0.4 \text{ m s}^{-1}$  to represent  
183 wind shear-related turbulence (Appendix A).

184 KASPR PPI measurements at an elevation angle of  $15^\circ$  (approximately every 7 minutes) are  
185 used to estimate wind direction and speed using a velocity-azimuth display (VAD) technique  
186 (Browning and Wexler, 1968). Using the VAD data up to maximum height of 7.8 km AGL, we  
187 estimated the vertical wind shear ( $W_{shear}$ ):

188 
$$W_{shear} = \sqrt{(u_{z_2} - u_{z_1})^2 + (v_{z_2} - v_{z_1})^2} / (z_2 - z_1) \quad (1)$$

189 where  $z$  represents height and  $u_z$  and  $v_z$  represent horizontal wind components at  $z$ . We use a 100  
 190 m (124 m for the Jan 4 case) spacing to estimate  $W_{shear}$  at each VAD data point ( $z_2 - z_1 =$   
 191 100 m). Since only a single elevation angle is used for the VAD, the resulting horizontal wind  
 192 profile is based on an increasing diameter cone with increasing height (~7.5 km diameter for 1 km  
 193 altitude and ~59.7 km for 8 km altitude). The moist Richardson Number (mRi) is calculated using  
 194 the following equation (Markowski and Richardson, 2010):

195 
$$mR_i = \frac{\frac{g}{\theta_e} \frac{\Gamma_m}{\Gamma_d} \frac{\Delta\theta_e}{\Delta z}}{\left(\frac{\Delta u}{\Delta z}\right)^2 + \left(\frac{\Delta v}{\Delta z}\right)^2} \quad (2)$$

196 where  $\theta_e$  is equivalent potential temperature,  $\Gamma_d$  and  $\Gamma_m$  are adiabatic lapse rate and pseudo  
 197 adiabatic lapse rate, respectively, and  $g$  is Earth's gravity.  $\theta_e$  and  $\Gamma_m$  were estimated from the  
 198 nearest soundings.  $u$  and  $v$  are horizontal wind components, which can be obtained from soundings  
 199 or the KASPR VAD measurements.

200

201 *b. Sounding and WSR-88D radar data*

202 Twice-daily radiosonde data at 0000 and 1200 UTC from the nearest NWS site (OKX; red  
 203 square in Fig.1), which is ~21 km to the east of Stony Brook. For the events in 2020 and 2021  
 204 additional soundings were launched every ~3 hours using the GRAW sounding system installed  
 205 on a Stony Brook University (SBU) mobile radar truck. The SBU mobile radar truck was deployed  
 206 in several locations in Long Island including Cedar Beach (40.965N, -73.030E; blue triangle in  
 207 Fig. 1; for 18 January 2020) and Stony Brook University (40.897N, -73.127E; green triangle in  
 208 Fig. 1; for 17 December 2020 and 1 February 2021).

209 To provide the regional precipitation context for these snow events, we used the radar  
 210 reflectivity from the NEXRAD WSR-88D surveillance scans at the lowest two elevation angles  
 211 (i.e., 0.5 and 0.8°) at the KOKX site.

212

213 *c. Ground-based in-situ measurements*

214 The Multi-Angle Snowflake Camera (MASC) was located at Stony Brook. The MASC consists  
 215 of three cameras that are separated by an angle of 36° and records hydrometeor particles larger  
 216 than 0.1 mm falling through the trigger field of 3100 mm<sup>2</sup> (Garrett et al. 2012; 2014). MASC was

217 only available for the January 2018 event. We also took photos of snowflakes using a digital single-  
 218 lens reflex (SLR) camera at Stony Brook, similar to Stark et al. (2013). We also used the snowfall  
 219 amount data from the Community Collaborative Rain, Hail, and Snow Network (CoCoRaHS;  
 220 Reges et al. 2016).

221

222 *d. Reanalysis data*

223 To examine the environment and frontogenesis during the snowstorm events, we used Rapid  
 224 Refresh reanalysis data (RAP), which is the National Oceanic Atmospheric administration hourly-  
 225 updated assimilation/modeling system operational at National Centers for Environmental  
 226 Prediction (Benjamin et al. 2016) with 37 pressure levels at the 13.5-km-resolution.

227 To track cyclone centers, we also used the mean sea level pressure from ERA5, which  
 228 combines 4D-VAR data assimilation and forecasts from the European Centre for Medium-Range  
 229 Weather Forecasts (ECMWF). ERA5 provides hourly data interpolated into 37 pressure levels at  
 230 0.5 degree horizontal resolution.

231

232 **3. Snow Events**

233

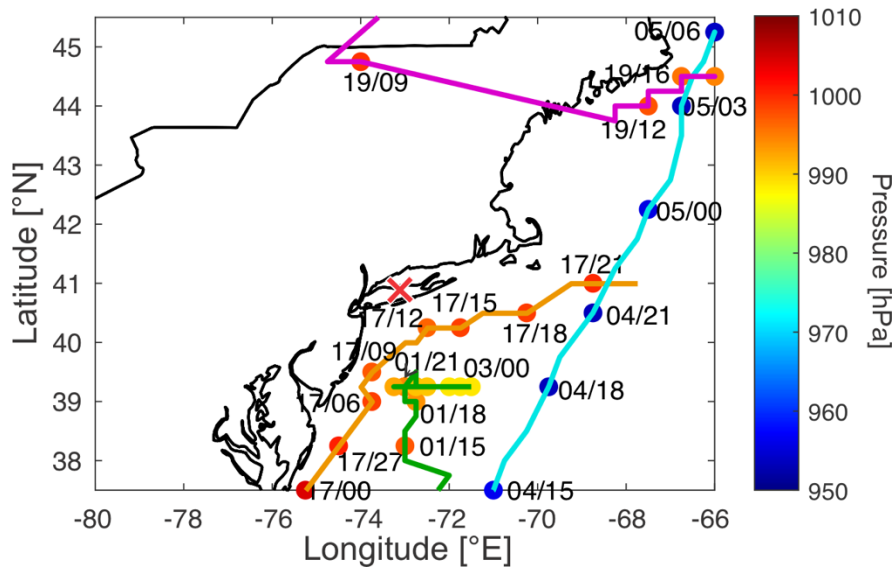
234 We examined four snowstorm cases: 4 January 2018; 18 January 2020; 16 – 17 December  
 235 2020; and 31 January to 1 February 2021. Three cases (4 January 2018; 16 – 17 December 2020;  
 236 and 31 January to 1 February 2021) had multi bands, while the other case (18 January 2020)  
 237 included a primary band. The cases were chosen to provide a diverse set of band structures within  
 238 the cyclone comma head. The track of the surface low pressure centers for the storms are shown  
 239 in Fig. 4. Table 1 summarizes storm characteristics and sample size for each case.

240

	Storm Quadrant	Types of bands within storm	Trend in storm Z intensity as it passed over Stony Brook (based on NEXRAD)	Period	Total cloudy time analyzed by VPT [min]	No. of VPT files used	No. of VAD profiles (PPI data files) used	Sounding time (day/hour) [UTC]
4 Jan 2018	S	Multi-bands	Sustain Z >30 dBZ	10:09 – 23:55 UTC	278.2	56	138	04/12, 05/00

18 Jan 2020	NW~W	Single-band	Weaken from 30 dBZ to < 25 dBZ.	14:10 – 23:59 UTC	196.7	80	80	18/12, 18/18, 18/19, 18/21, 19/00
16 – 17 Dec 2020	N~N W	Multi-bands	Sustain Z >30 dBZ	18:22 UTC on Dec. 16 – 02:59 UTC on Dec. 17	184.1	75	76	16/12, 17/00, 17/03
31 Jan –1 Feb 2021	N	Multi-bands	Weakening from 40 dBZ to 30 dBZ.	18:02 UTC on Jan. 31 – 23:51 UTC on Feb. 1	236.4	119	170	31/12, 01/00, 01/06, 01/08, 01/12, 01/15, 01/18, 01/21, 02/00

241  
242 Table 1. Summary of the storm characteristics and sample sizes. Soundings at 00 and 12 UTC are from the  
243 NWS OKX soundings, and the others are from the SB mobile truck.



244  
245 Figure 4: Tracks of the cyclone centers every hour using hourly ERA5 mean sea level pressure for the cases of  
246 4 Jan 2018 (blue line), 18 Jan 2020 (magenta line), 17 – 16 Dec 2020 (orange line), and 31 Jan –1 Feb 2021  
247 (green line). Color for each dot represents the surface central pressure (in hPa) every three hours. Cross mark  
248 represents the Stony Brook location.  
249

250 *a. 4 January 2018*

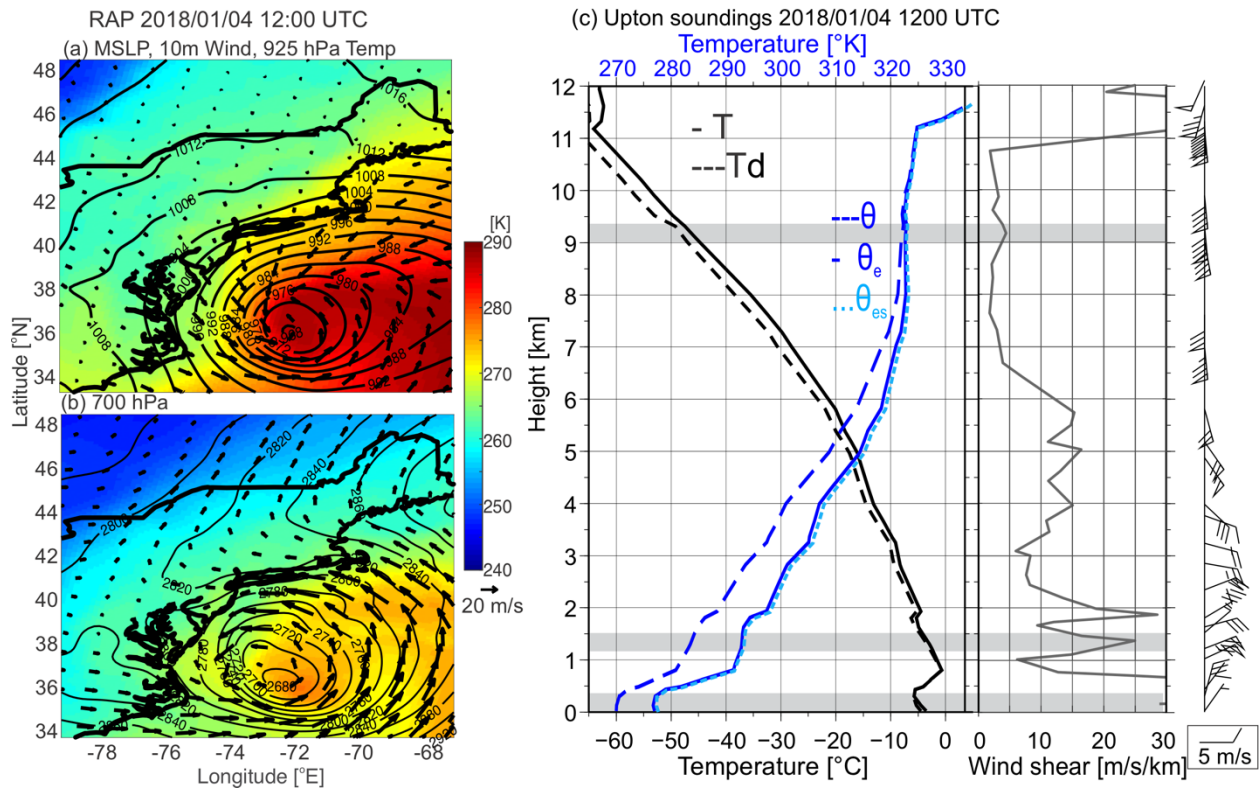
251 At 1200 UTC 4 January 2018, a deep surface cyclone (~968 hPa) is located a few hundred  
252 kilometers to the southeast of Long Island, NY (Fig. 5a). There is a strong temperature gradient at  
253 925 hPa extending to the north of the cyclone just south of Long Island. At 700 hPa (Fig. 5b),  
254 southeasterly wind with the closed low results in warm advection extending northward to Long

255 Island. The NWS sounding at 1200 UTC on 4 January shows a gradual wind veering from  
256 northeasterly below 2.5 km above mean sea level (ASL) to southerly at 6-km ASL (Fig. 5c), while  
257 there is a stable layer with a shallow frontal zone from 0.4-0.8 km ASL. From Eq. 1, there are  
258 relatively large vertical wind shear layers ( $> 15 \text{ m s}^{-1} \text{ km}^{-1}$ ) below 6 km ASL. They generally  
259 correspond to heights of large gradient of temperature and  $\theta_e$ , and a few of them correspond to the  
260  $\text{mRi} < 0.25$  (indicated by gray shades in Fig. 5c). The vertical profile is less stable and near moist  
261 neutral from 7-10 km ASL.

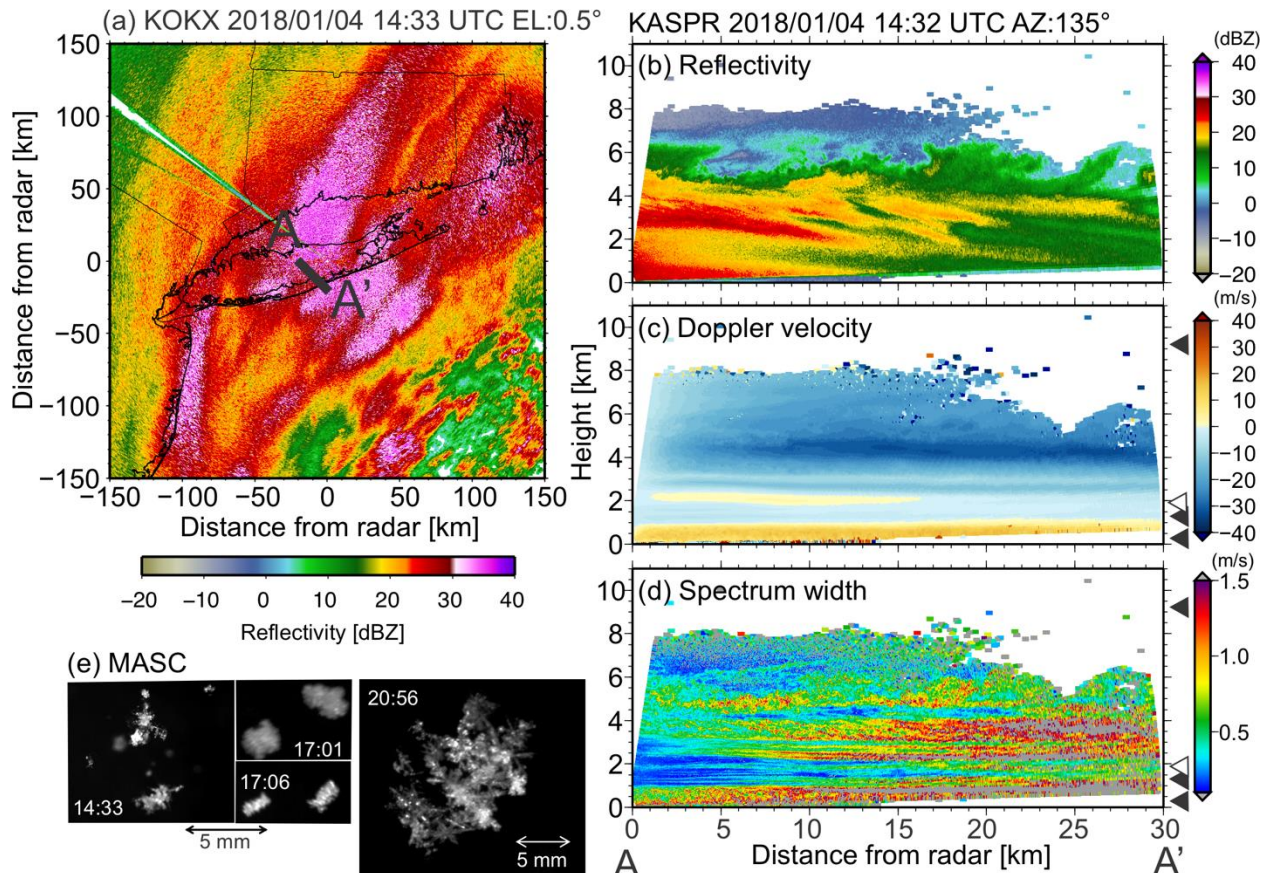
262 As the storm center moves from south of Long Island to the northeast (blue track in Fig. 4),  
263 the snowbands within the comma head produce heavy snow across Long Island from 1000 UTC 4  
264 January to 0100 UTC 5 January 2018, with CoCoRaHS reporting the maximum 24-hour  
265 precipitation of 59 mm (~30 cm depth) across central Long Island. From 0900-1240 UTC, narrow  
266 snowbands (to 25 dBZ) orientated north-northeast to south-southwest crossed Stony Brook (not  
267 shown), about 300 km northwest of the surface cyclone (Fig. 4). The MASC recorded compact,  
268 tiny ( $< 1\text{-}2 \text{ mm}$ ) ice particles that were heavily rimed (not shown, but similar to Fig. 6e). The  
269 snowbands are further intensified to  $> 35 \text{ dBZ}$  by 1740 UTC 4 January (Figs. 6a,c,d,e), when the  
270 cyclone center becomes closer to Stony Brook (Fig. 4). The surface snow habits are heavily rimed,  
271 with larger sizes of 3-5 mm and partially-rimed columnar crystals than during the earlier snowband  
272 period (Fig. 6e).

273 The KASPR RHI measurements across the snowbands at 1432 UTC ( $135^\circ$  in azimuth, Fig. 6b)  
274 reveal individual cells between 4-7 km altitudes and fallstreaks underneath. This convective cell  
275 layer at 4-7 km is collocated with a relatively large SW of approximately  $0.4 \text{ m s}^{-1}$ . Although the  
276 SW from lower elevation scans could include more contributions of horizontal wind shear than  
277 turbulence (Appendix A), the large SW in the convective cell layer even at higher elevation angle  
278 suggests a presence of strong turbulence. Black and white triangles in Fig. 6c and 6d represent the  
279 centered heights of the shear unstable layers with  $\text{mRi} < 0.25$  and layers with vertical wind shear  
280  $> 20 \text{ m s}^{-1} \text{ km}^{-1}$  with  $\text{mRi} > 0.25$ , respectively observed by the sounding shown in Fig. 5c (note  
281 that most of black triangles include the vertical wind shear  $> 20 \text{ m s}^{-1} \text{ km}^{-1}$ ). The larger SW layers  
282 in the RHI scans include contributions from turbulence, wind shear, and cross wind (Eq. A1 in  
283 Appendix A), and the wind shear contribution can be more significant at lower elevation angles as  
284 the SW layers are roughly consistent with the vertical wind shear shown in the RHI Doppler  
285 velocity A-A' (Fig. 6c) and sounding profile (Fig. 5c).

286 The snowband pivots and changes its motion from westward to eastward around 1730 UTC  
 287 (not shown), as the cyclone center moves ~500 km southeast of Long Island (Fig. 4). The  
 288 snowbands pass over Stony Brook from west to east around 2030-2100 UTC. The dominant snow  
 289 particles at the surface are large aggregates (> 5 mm), which include less rimed needles and  
 290 branched crystals (e.g., Fig. 6e at 2056 UTC). After the passage of the snowband, several relatively  
 291 weak reflectivity bands < 25 dBZ, oriented along north-to-south or north-northwest-to-south-  
 292 southeast pass through Stony Brook until 0200 UTC on 5 January 2018.



293  
 294  
 295 Figure 5: (a) Mean sea level pressure (contour), temperature at 925 hPa, and horizontal wind (arrows). (b) 700-  
 296 hPa temperature (color shade), geopotential height (contour) and horizontal wind (arrows) from RAP  
 297 reanalysis data at 14 UTC on 4 Jan 2018. (c) Sounding profiles of temperature (black solid line), dew point  
 298 temperature (black dashed line), potential temperature ( $\theta$  blue dashed line), equivalent potential temperature  
 299 ( $\theta_e$  blue solid line), saturated equivalent potential temperature ( $\theta_{es}$  light blue dashed line), and vertical wind  
 300 shear estimated from Eq. 1 (gray line in the right panel) at 1200 UTC from OKX. Gray shaded layers in (c)  
 301 represent layers of moist Richardson Number (mRi) < 0.25.  
 302



303  
 304 Figure 6: (a) Horizontal distribution of KOKX reflectivity from a PPI scan at an elevation angle of 0.5° at 1433  
 305 UTC on 4 Jan 2018, and vertical cross sections of KASPR (b) reflectivity (shaded in dBZ), (c) mean Doppler  
 306 velocity in  $\text{m s}^{-1}$ , (d) Doppler spectrum width in  $\text{m s}^{-1}$  from RHI scan along A-A' line in (a) at 1432 UTC, and  
 307 (e) photos of snowflakes taken by MASC at 1433 UTC, 1701 UTC, 1706 UTC, and 2056 UTC. Positive sign  
 308 of KASPR Doppler velocity represents away from the radar. Black and white triangles on right axis in (c) and  
 309 (d) represent the shear unstable layers ( $\text{mRi} < 0.25$ ) and vertical wind shear  $> 20 \text{ m s}^{-1} \text{ km}^{-1}$  that are linked to  
 310  $\text{mRi} > 0.25$  from the sounding in Fig. 5c (note that most of black triangles include the vertical wind shear  $> 20$   
 311  $\text{m s}^{-1} \text{ km}^{-1}$ ).

312  
 313

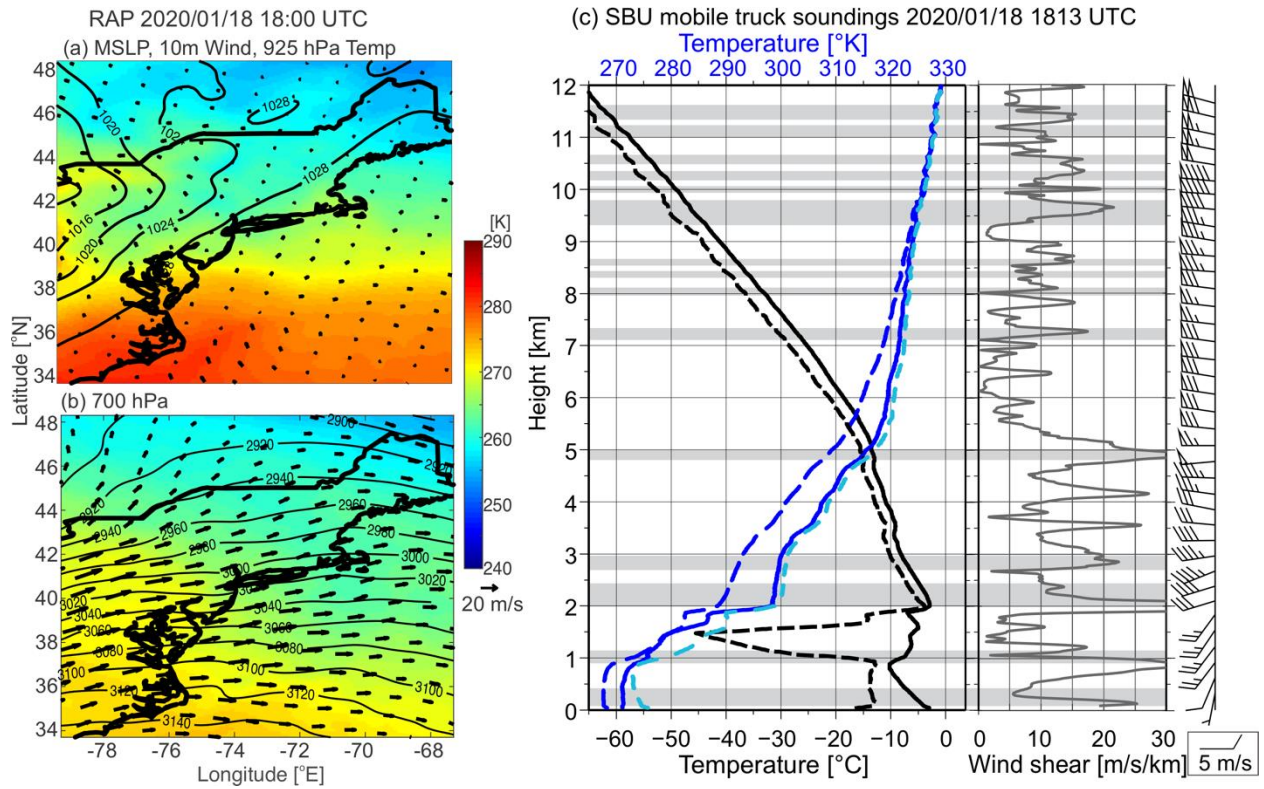
#### 314 *b. 18 January 2020*

315 At 1500 UTC 18 January 2020, a surface cyclone ( $\sim 1003 \text{ hPa}$ ) is centered over northern  
 316 Michigan (not shown). By 0300 UTC 19 January (Fig. 7a), the associated surface warm front is  
 317 southwest of Long Island along the mid-Atlantic coast as the storm center moves eastward  
 318 (magenta track in Fig. 4). There is 700-hPa warm advection from Long Island southwestward (Fig.  
 319 7b). The sounding from the SBU mobile truck at 1813 UTC 18 January, which is closest to the  
 320 snowband passage, shows a warm-frontal stable layer with veering winds from 1-2 km ASL and a  
 321 near moist neutral layer from 2-3 km ASL (Fig. 7c). The sounding and radar measurements suggest  
 322 that the cloud top height exceeded 10 km ASL. The sounding shows more layers of vertical wind

323 shear compared to the 4 January case (Fig. 5c), probably due to frequent samples of data  
324 (approximately every 5 m). In the cloud layer between 2 and 10 km, the vertical wind shear layers  
325 ( $> 20 \text{ m s}^{-1} \text{ km}^{-1}$ ) are collocated with shear unstable layers ( $\text{mRi} < 0.25$ , gray shades) except at 3.5  
326 and 4.2 km. A warm-frontal snowband ( $> 20 \text{ dBZ}$ ) orientated from northwest to southeast crossed  
327 Stony Brook between 1830-2015 UTC 18 January (Fig. 7c). The maximum WSR-88D reflectivity  
328 for this snowband ( $\sim 30 \text{ dBZ}$ ) is 5-10-dB weaker than the other cases. The CoCoRaHS suggests  
329 liquid-equivalent precipitation of  $\sim 10 \text{ mm}$  ( $\sim 6.4 \text{ cm}$  snow depth) at Stony Brook over 24 h ending  
330 at 0200 UTC on 19 January. After the snowband passed Stony Brook, the WSR-88D reflectivity  
331 weakens to  $< 25 \text{ dBZ}$ . The surface precipitation transitions to rain after the warm frontal snowband  
332 passage and there are more embedded convective cells  $> 20 \text{ dBZ}$  (not shown). This study focuses  
333 on the warm frontal snowband to avoid uncertain errors associated with hydrometeor attenuation  
334 in the rain layer.

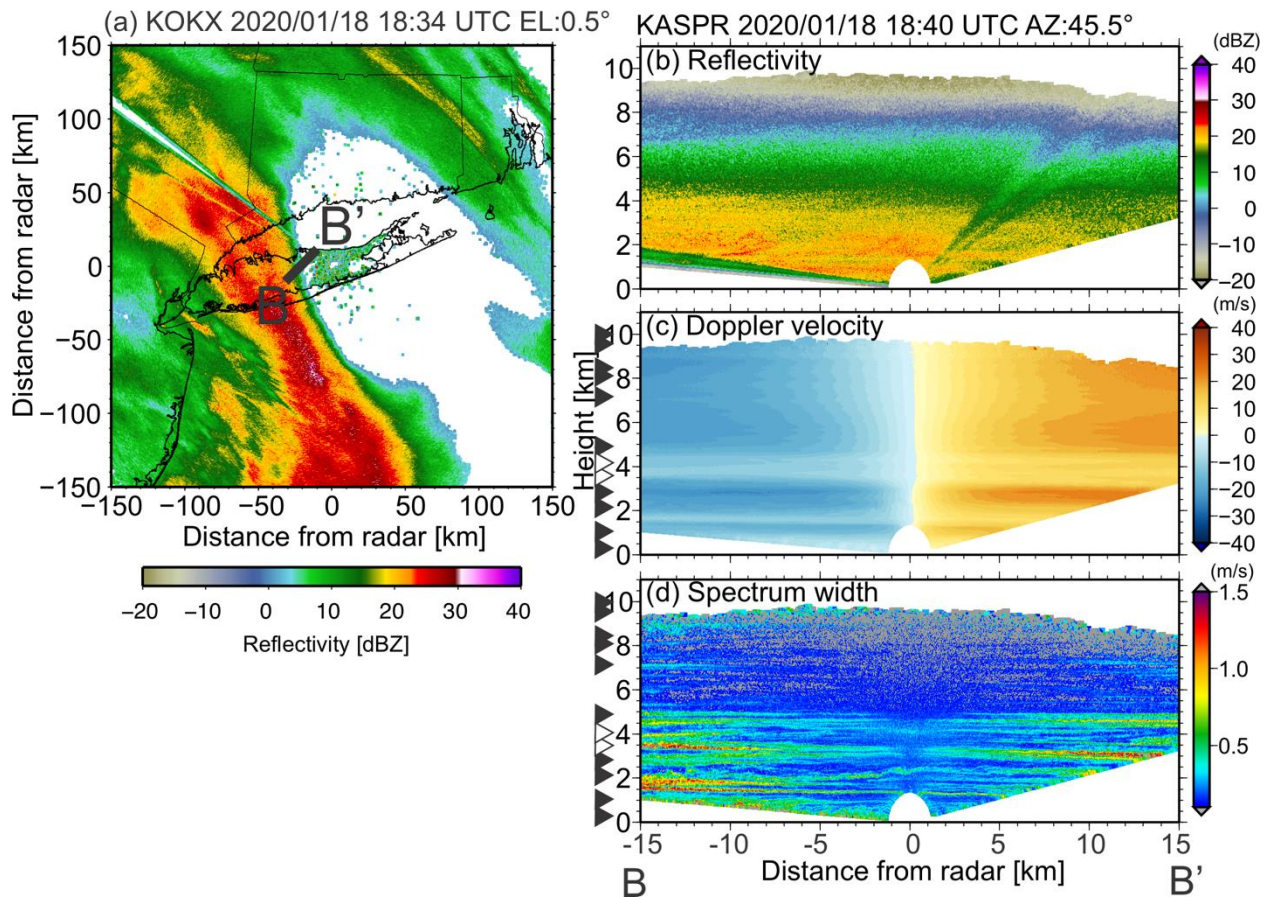
335 KASPR RHI scans oriented NE-SW (B-B' in Fig. 8a) and crossing the snowband (Figs. 8b-d)  
336 reveal relatively uniform reflectivity at a given altitude and a gradual vertical gradient in  
337 reflectivity that intensifies towards the surface associated with the snowband. The cloud top  
338 reaches 9.5 km ASL, and the SW is  $\sim 0.3 \text{ m s}^{-1}$  near the cloud top. Considering the weak wind shear  
339 in the Doppler velocity field in Fig. 8c and weak reflectivity echoes which can have narrower  
340 particle size distributions, these SW values suggest turbulence (or weak updraft) signatures within  
341 some convective cells. The shear unstable layers at around 2.5 and 5 km shown in Fig. 7c roughly  
342 correspond to vertical intensifications of KASPR reflectivity in the RHI measurements (Fig. 8b).  
343 Unfortunately, the MASC was not functional during the event, but KASPR polarimetric signatures  
344 and Doppler velocity from the VPT measurements suggest aggregates with little riming below 7  
345 km altitude (not shown).

346



347  
 348  
 349  
 350  
 351

Figure 7: Same as Fig.5 but (a,b) at 1500 UTC and (c) launched at 1813 UTC on 18, Jan 2020. The sounding data were collected at Cedar Beach.



352  
 353 Figure 8: Same as Fig.6 but (a) at 1834 UTC and RHIs (b-d) along B-B' line in (a) at 1840 UTC on 18 Jan  
 354 2020. The sounding data were collected at Cedar Beach (blue triangle in Fig. 1).  
 355  
 356

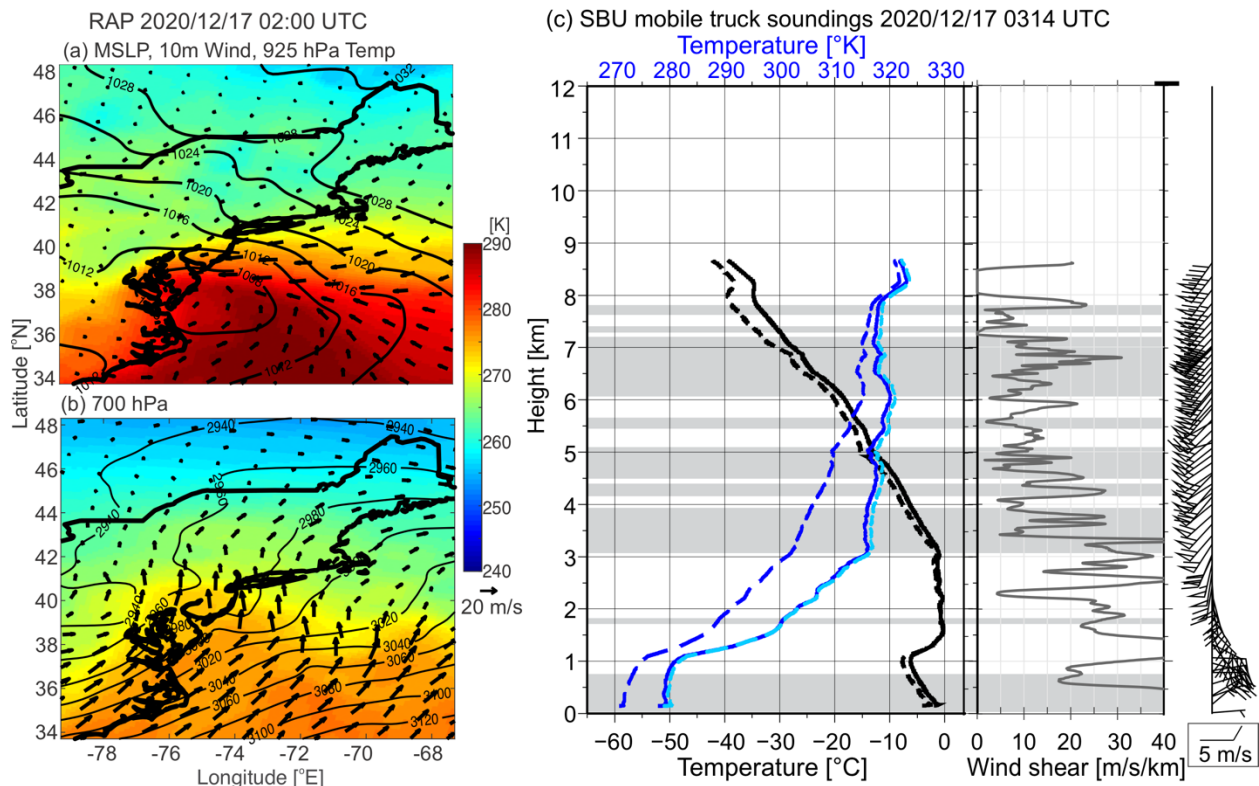
357 *c. 16-17 December 2020*

358 At 0200 UTC (Fig. 9a), surface low pressure (~1006 hPa) is along the mid-Atlantic coast and  
 359 moves northward offshore during the next 24 h (orange track in Fig. 4). A well-defined warm front  
 360 exists to the north of the surface cyclone stretching from west to east south of Long Island (Fig.  
 361 9a), with warm advection at 700 hPa over Long Island (Fig. 9b). The WNW-ESE oriented  
 362 snowbands exceeding 30 dBZ cross Long Island from 2220 UTC 16 December to 1000 UTC 17  
 363 December. The maximum 24-h precipitation (water equivalent) is 44 mm by 1200 UTC 17  
 364 December at Nesconset (~8 km southwest of Stony Brook, not shown). The Stony Brook surface  
 365 temperature was below freezing until 0900 UTC 17 December, while soundings at 0000, 0606,  
 366 and 0715 UTC 17 December at Stony Brook show an inversion layer and a temperature > 0°C  
 367 centered around 1.5, 2.3, and 2.4 km ASL, respectively. KASPR RHI shows a melting layer after  
 368 0350 UTC 17 December at 2.5 km ASL. We focus on the period prior to the melting signature.

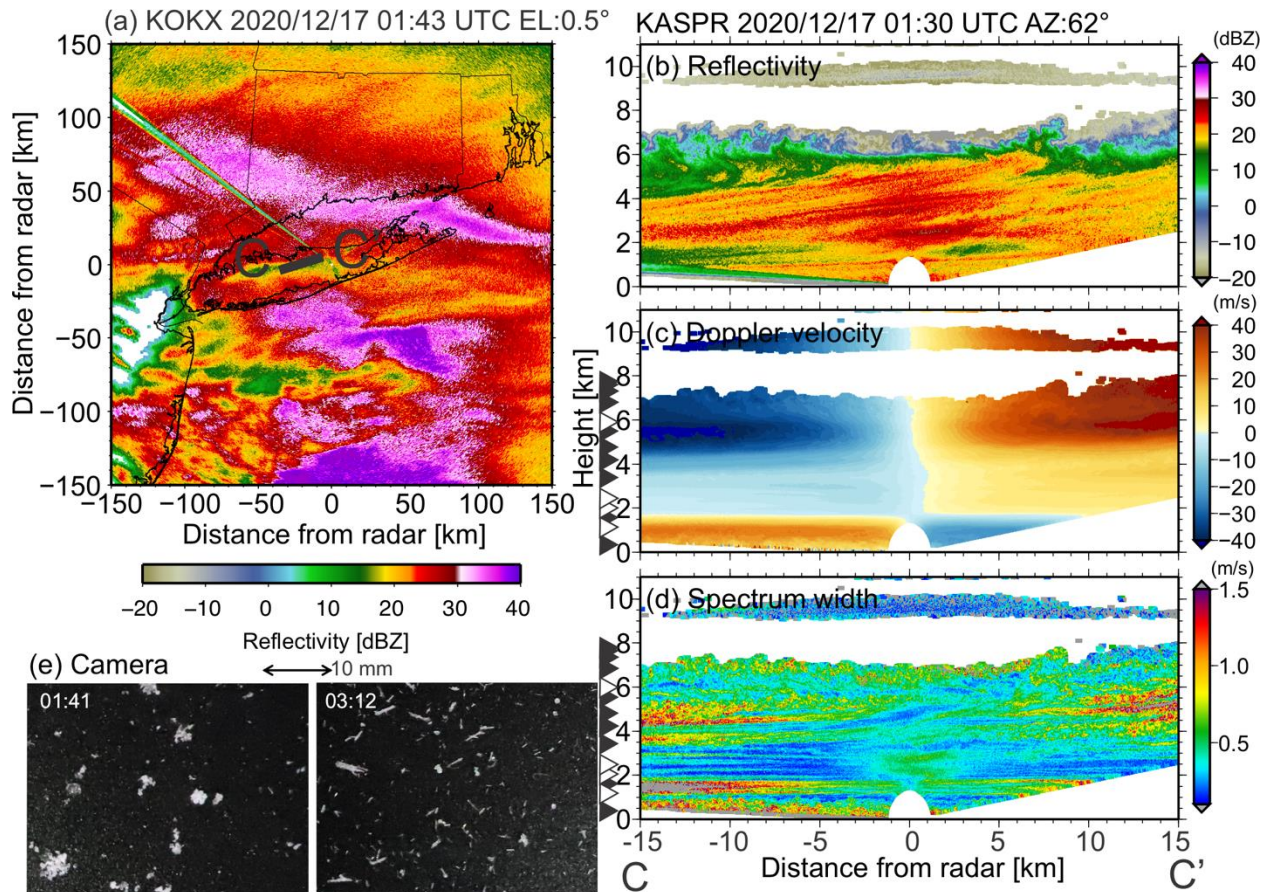
369 The sounding at 0314 UTC 17 December has vertical wind shear layers ( $> 20 \text{ m s}^{-1} \text{ km}^{-1}$ ), most of  
 370 which above 3 km ASL are linked to  $\text{mRi} < 0.25$ .

371 The snowbands pass over Stony Brook from south to north from 0000 to 0310 UTC (Fig. 10a).  
 372 There are generating cells in the KASPR RHI at cloud top, with areas of relatively large SW ( $>$   
 373  $0.75 \text{ m s}^{-1}$ ) from 6-7.5 km ASL, and fallstreaks extending downward to the west below 6 km ASL  
 374 (Figs. 10b-d) which are modified by the wind shear at around 5.4 km ASL (Fig. 9c). The cloud top  
 375 cells are in a moist neutral stable layer with supersaturation with respect to ice (Fig. 9c). Although  
 376 layers with  $\text{SW} > 1.3 \text{ m s}^{-1}$  in the RHI SW plot (Fig. 10d) are well consistent with the Doppler  
 377 velocity shear layers (Fig. 10c), they are also roughly consistent with the shear unstable layers  
 378 shown in Fig. 9c (gray shades in Fig. 9c and black triangles in Fig. 10). The shear unstable layers  
 379 above 3 km shown in Fig. 9c (gray shades) correspond to the generating cells in the RHI plot. The  
 380 SLR camera at Stony Brook (operated from 0030 to 1254 UTC on 17 December) shows rimed  
 381 crystals, including sector plates and needles at 0030-0225 UTC, primarily needle crystals at 0230-  
 382 0400 UTC (Fig. 10e), and some refrozen particles are included from 0426 to 0548 UTC (not  
 383 shown).

384



385  
 386 Figure 9: Same as Fig.5 but (a,b) at 0200 UTC on 17 Dec, 2020 and (c) at 0314 UTC on 17 Dec 2020. The  
 387 sounding data were collected at Stony Brook (green triangle in Fig. 1).



389  
 390 Figure 10: Same as Fig.6 but (a) at 0143 UTC, (b-d) RHIs along C-C' line in (a) at 0130 UTC on 17 Dec 2020,  
 391 and (e) taken by the SLR camera at Stony Brook.  
 392  
 393

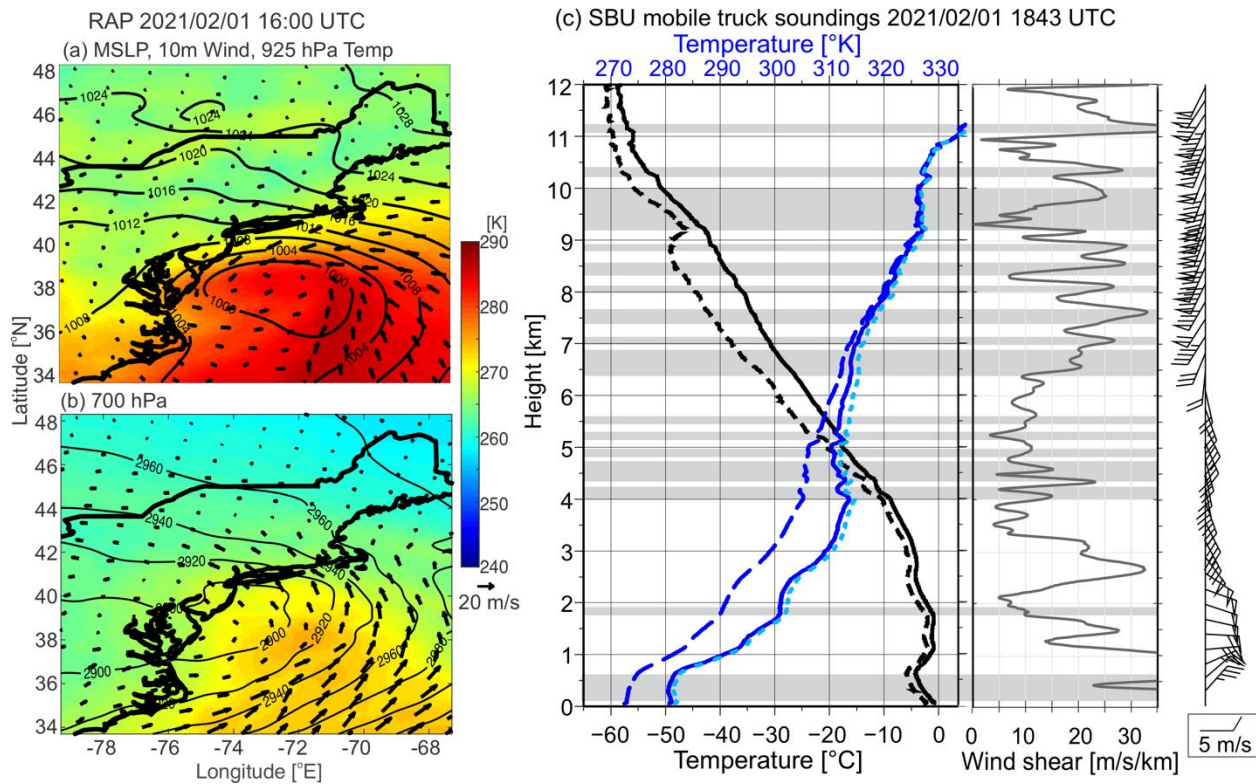
394 *d. 1 February 2021*

395 Similar to 16-17 December, the snow event on 31 January to 1 February 2021 is also associated  
 396 with a surface cyclone moving northward to the south of Long Island (green track in Fig. 4, Figs.  
 397 11-12). We call this event the 1 February 2021 since most of the precipitation period was observed  
 398 on 1 February 2021 at Stony Brook. There is a surface warm front just south of Long Island, with  
 399 warm advection at 700 hPa over this region (Figs. 11a,b). Surface precipitation started at 0217  
 400 UTC at Stony Brook, with a maximum 24-h precipitation of 56 mm by 0200 UTC 2 February at  
 401 Stony Brook. The Stony Brook sounding at 1843 UTC 1 February shows that most of the vertical  
 402 wind shear layers ( $> 20 \text{ m s}^{-1} \text{ km}^{-1}$ ) correspond to shear unstable layers ( $\text{mRi} < 0.25$ , gray shades)  
 403 above 4 km. A moist unstable layer exists near cloud top (4-5.2 km ASL). No snowbands were  
 404 apparent around Long Island before 0210 UTC 1 February (not shown). After 0210 UTC 1  
 405 February, there are precipitation areas with reflectivity  $> 30 \text{ dBZ}$  around Stony Brook, but they

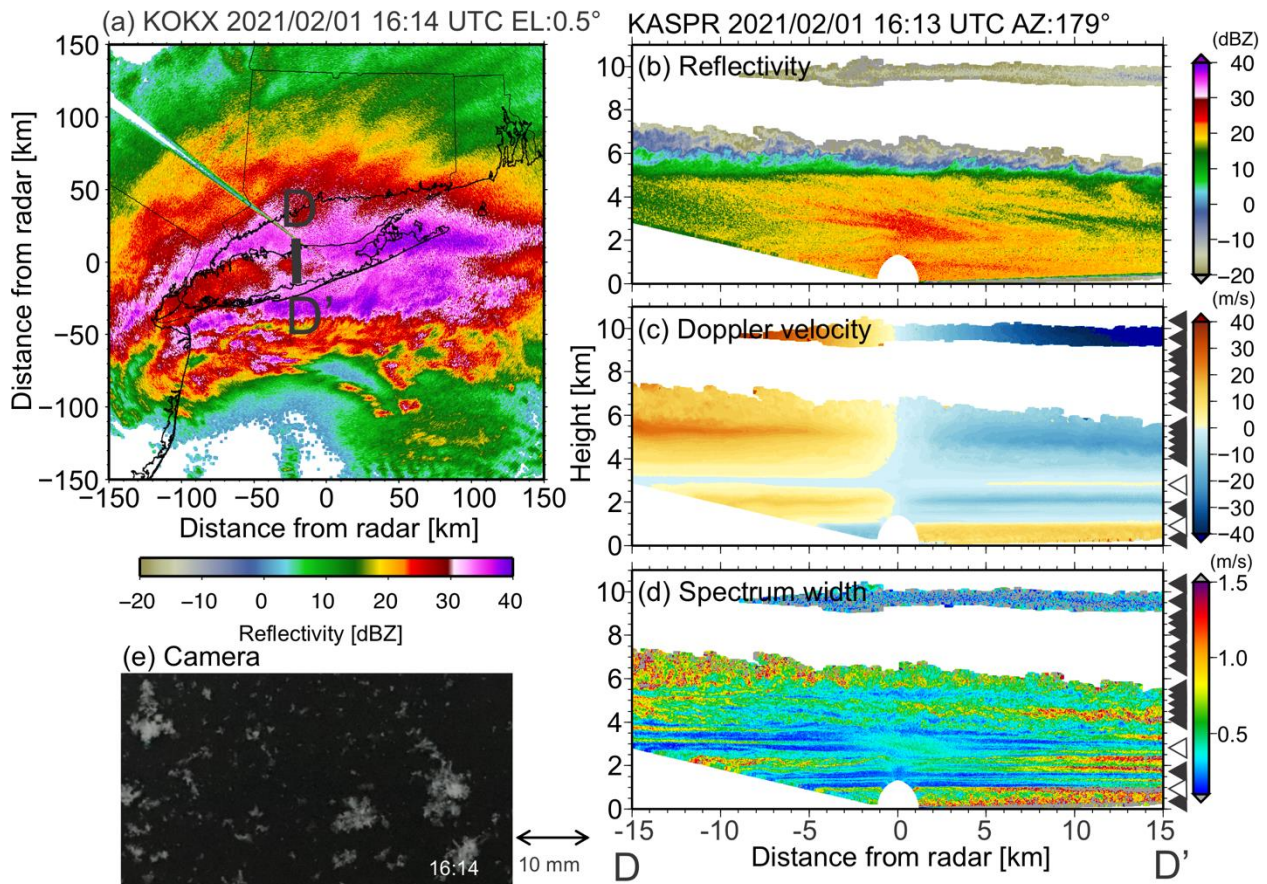
406 are not banded until 1300 UTC 1 February. From 1400 UTC to 1830 UTC 1 February, two west-  
 407 east oriented snowbands (30-40 dBZ) cross Stony Brook moving northward (Fig. 12a). There are  
 408 cloud-top generating cells at 5.2-7.5 km ASL and fallstreaks to 25 dBZ underneath the generating  
 409 cell layer during the snowband period (Fig. 12b). The dBZ difference between the WSR-88D and  
 410 KASPR is likely owing to non-Rayleigh scattering at Ka-band reflectivity, indicating the presence  
 411 of large snow particles. The Stony Brook sounding at 1843 UTC 1 February for the generating cell  
 412 layer includes moist instability, wind shear, and supersaturation with respect to ice (Fig. 11c).

413 Black and white triangles in Figs. 12c and 12d represent the centered height of the shear  
 414 unstable layers ( $mRi < 0.25$ ) and vertical wind shear ( $> 20 \text{ m s}^{-1} \text{ km}^{-1}$ ) with  $mRi < 0.25$ ,  
 415 respectively, observed by the sounding in Fig. 11c. Large SW near the radar echo top height well  
 416 collocate with the generating cells and also the moist unstable layer. Layers with  $SW > 0.4 \text{ m s}^{-1}$   
 417 in the RHI SW plot (Fig. 12d) are well consistent with the Doppler velocity shears (Fig. 12c), and  
 418 those below 6 km are roughly consistent with the vertical wind layers and shear unstable layers in  
 419 Fig. 11c. The MASC was not functional during the event, but the SBU SLR camera's photos show  
 420 partially-rimed aggregates of plate-like and needle crystals during the main snowband period  
 421 (1058 - 2055 UTC 1 February, Fig. 12e).

422



424 Figure 11: Same as Fig.5 but (a,b) at 1600 UTC on 1 Feb, 2020 and (c) launched at 1843 UTC on 1 Feb, 2021.  
 425



426 Figure 12: Same as Fig.6 but (a) at 1614 UTC on 1 Feb 2021, (b-d) RHIs along D-D' line in (a) at 1613 UTC  
 427 on 1 Feb 2021, and (e) taken by the SLR camera at Stony Brook.  
 428  
 429  
 430

#### 4. Updraft Analysis Results

432

##### a. Characteristics of detected updraft regions

434 Table 2 lists the number of the URs detected within the cloud echo observed by the KASPR  
 435 VPT measurements, and those averaged per 5 minutes by the total cloudy time, which is defined  
 436 as an accumulated time where KASPR observed cloud echoes at any altitude during the analysis  
 437 period. The number of URs above 1.2 km above ground level (AGL) are also listed. The warm  
 438 frontal band case on 18 January 2020 has the lowest number of the updraft regions per 5 min  
 439 among the four cases (~10 per 5 min). The other cases have 2-5 times more URs. It is interesting  
 440 that the NWS sounding from the 4 January case had fewer layers of wind shear and low mRi than  
 441 the Stony Brook soundings from the other cases, which had higher data sampling rates, even

442 though the 4 January case produced larger number of URs. This may suggest that the URs could  
 443 be associated with thin layers of vertical wind shears, as observed by the SBU soundings and  
 444 KASPR RHI Doppler velocity and spectrum width measurements.

445 We identified the URs below ~1.2 km AGL for all cases. These are likely associated with the  
 446 boundary layer turbulence (Figs.5c, 7c, 9c, and 11c). To focus on updrafts which may have strong  
 447 relationships with storm evolution, wind shear, and shear-induced turbulence in clouds, we do not  
 448 include the boundary layer updraft regions in the present analysis.

449

450

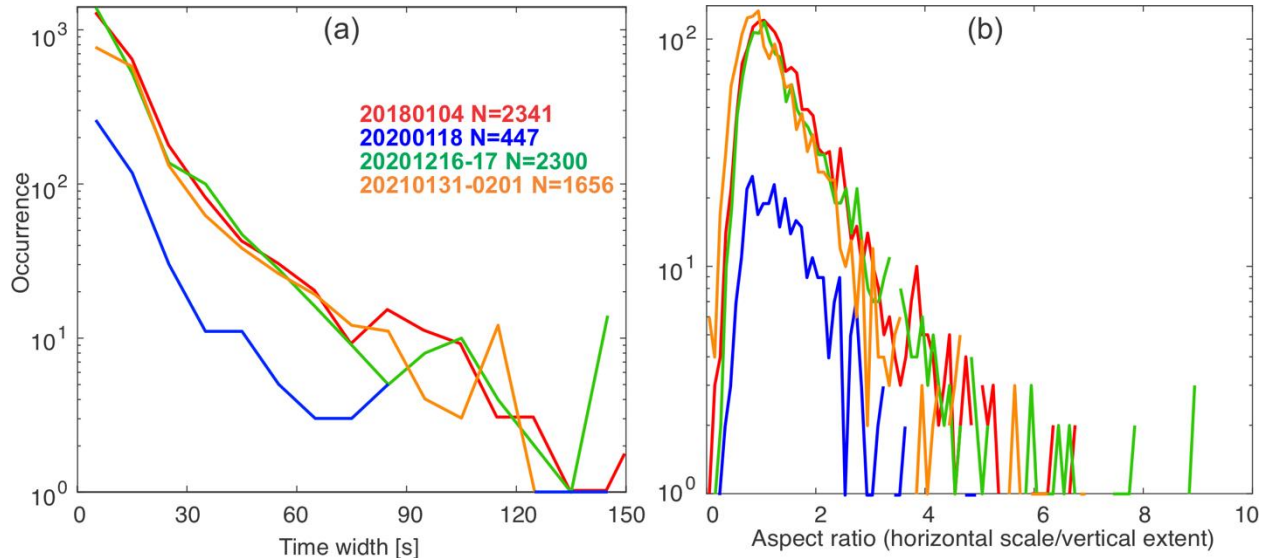
	Total number	Height > 1.2 km	Average Per 5 min	Average Per 5 min for height > 1.2 km	Number with SW > 0.4 m s <sup>-1</sup> for height > 1.2 km
Jan 4, 2018	3376	2341	60.7	42.1	728 (31.1%)
Jan 18, 2020	673	447	17.2	11.4	12 (2.7%)
Dec 16 – 17, 2020	2774	2300	75.3	62.5	667 (29.0%)
Jan 31 – Feb 1, 2021	2171	1656	45.9	35.0	528 (32.9%)

451 Table 2. The number of detected updraft regions in total and averaged per 5 minutes. The numbers of detected  
 452 updraft regions counted for heights > 1.2 km are also listed. The percentages in the parenthesis in the right most  
 453 column represents the those of the total number of URs for height > 1.2 km.

454

455 Figure 13a shows frequency distributions of the duration of URs detected above 1.2 km AGL  
 456 within a 10-sec interval. Even though the number of detected URs varies by event, the qualitative  
 457 characteristics of the duration time distribution is similar for all four cases. There is a peak at the  
 458 smallest size bin for the four cases, and overall, the number exponentially decreases with size.  
 459 Most of the updraft regions last for less than 20 sec (i.e., small size in the height-time plots), which  
 460 accounted for approximately 80% of the total. The maximum duration bin is 95 sec. This  
 461 distribution shape and qualitative features do not change when different thresholds are used for  
 462 mean Doppler velocity (Sect. 2a). The distribution curves from the three cases which had more  
 463 than 1600 updraft regions show similar exponential distribution. Considering that the horizontal  
 464 extent of UR can be roughly estimated as duration × horizontal wind speed estimated from the  
 465 KASPR VAD, approximately 85% of URs have the horizontal scale < 500 m. The mean vertical  
 466 extent of URs is 261 m for all cases, and more than 81% of URs have depths less than 330 m. The

467 aspect ratio of the URs (defined as the ratio of the horizontal scale to the vertical extent) for each  
 468 case shown in Fig. 13b has a lognormal frequency distribution with the frequency peak around 1.

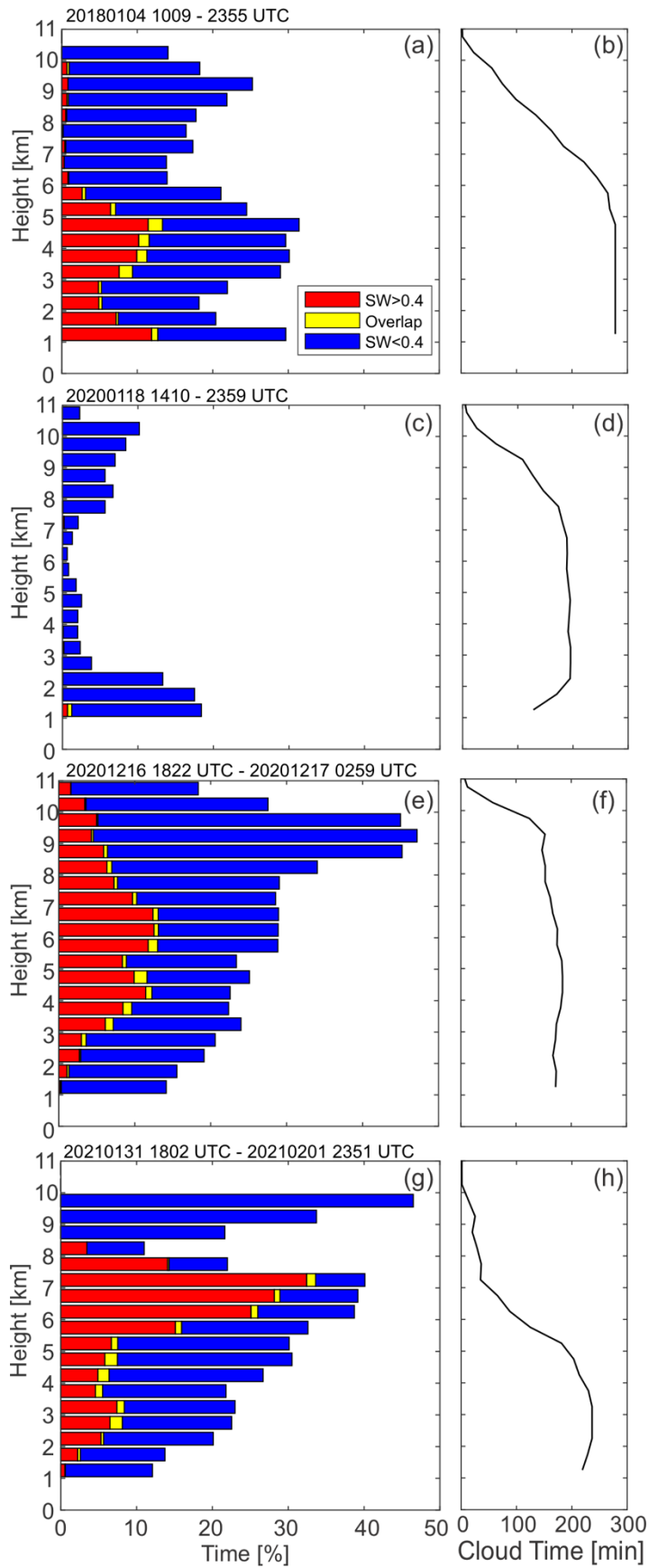


469 Figure 13: Distributions of (a) time-width of the URs with the time bin size of 10 s for 4 Jan 2018 (red), 18 Jan  
 470 2020 (blue), 16 – 17 Dec 2020 (green), and 31 Jan – 1 Feb 2021 (orange) and (b) aspect ratio of the URs  
 471 defined as the ratio of horizontal scale to the vertical extent. The time width for each updraft region is defined  
 472 as the time between the time when the updraft region appeared first and the time when it disappeared. The  
 473 horizontal scale is estimated using the time width and the horizontal wind speed estimated from the KASPR  
 474 VAD measurements. The sample size for each case is shown in the right corner in (a).  
 475  
 476

477  
 478 Figure 14 shows the vertical distributions of the URs. The total length of each bar is the  
 479 accumulated time with updrafts divided by the accumulated time with cloud echo as a percent at  
 480 each altitude bin (0.5 km). We classified the regions for smaller and larger spectrum width (SW)  
 481 from the KASPR VPT measurements with a threshold of  $0.4 \text{ m s}^{-1}$ , shown by color-coded subsets  
 482 along each bar (UR with  $\text{SW} < 0.4 \text{ m s}^{-1}$  named URSWLO and UR with  $\text{SW} > 0.4 \text{ m s}^{-1}$  named  
 483 URSWHI). Higher values of  $\text{SW} > 0.4 \text{ m s}^{-1}$  can be a proxy for higher magnitudes of turbulence  
 484 (Appendix A). For the three multi snowband cases, URs collocated with  $\text{SW} > 0.4 \text{ m s}^{-1}$   
 485 (URSWHIs) accounted for approximately 30% of the total number of URs above 1.2 km height  
 486 (Table 2), while for the January 18 case URSWHIs only accounted for 3%. The UR accounts for  
 487 more than 50% of cloud echo time at almost all levels for the three multi-band cases and less than  
 488 or equal to 10% above 2.5 km for the single-band 18 Jan 2020 case (Fig. 14).

489 Although there is a case to case variability in the heights, URSWHIs, occurred in more interior  
 490 clouds of the multi snowband cases. URSWHIs tend to be shorter lived compared to the  
 491 URSWLOs for all cases (approximately 1 – 2 sec shorter, Table 3). URSWHIs have slightly (0.08

492 – 0.15 m s<sup>-1</sup>) stronger median upward motion and 4.2 – 16.4 dB larger median reflectivity (Table  
493 3). In contrast, URs collocated with SW < 0.4 m s<sup>-1</sup> (URSWLOs) show higher frequencies at higher  
494 altitudes, near cloud tops. It is possible that the updrafts at the cloud tops could be produced in part  
495 by instabilities caused by cloud-top radiative cooling. The URs have a median thickness of 150 –  
496 240 m. The URSWHIs are thicker than URSWLOs for all cases, but the difference varies between  
497 0 m (16 – 17 December) and 90 m (18 January). Considering the range-gate spacing for the VPT  
498 measurements, the difference in the number of range-gates for the thickness is less than 6. These  
499 qualitative characteristics do not change significantly when the Doppler velocity threshold for the  
500 detection is changed to 0.2 and 0.6 m s<sup>-1</sup>.  
501



503 Figure 14: (a,c,e,g) Histograms of occurrence (time relative to the total cloudy time observed by KASPR VPT)  
 504 of detected updraft regions shown as percentage of the entire cloud echo time at each altitude for the cases of 4  
 505 Jan 2018, 18 Jan 2020, 16 – 17 Dec 2020, and 1 Feb 2021, respectively. The color bars represent different  
 506 magnitudes of mean Doppler spectrum width (SW) with a shear threshold (red:  $SW > 0.4 \text{ m s}^{-1}$  and blue:  $SW <$   
 507  $0.4 \text{ m s}^{-1}$ ). The SW from the KASPR VPT measurements was averaged over each updraft region. The 15-m  
 508 vertical resolution data were resampled every 0.5 km height. In a resampled 0.5 km height range, some URs  
 509 located in different heights can be overlapped in time. Periods where UR having  $SW > 0.4 \text{ m s}^{-1}$  and UR having  
 510  $SW < 0.4 \text{ m s}^{-1}$  are overlapped in time are represented by yellow bars. (b,d,f,h) Profiles of the time used for the  
 511 analysis at each height bin. The analysis was based on the VPT scans for 3 min duration every 8 minutes (5-min  
 512 duration every 15 minutes for the 2018 case). The analysis periods are displayed and also shown in Table 1.  
 513

514

	Median duration (sec)		Median thickness (m)		Median upward motion ( $\text{m s}^{-1}$ )		Median reflectivity (dBZ)	
	URSWHI	URSWLO	URSWHI	URSWLO	URSWHI	URSWLO	URSWHI	URSWLO
4 Jan 2018	7.2	9.3	165	150	0.62	0.50	15.85	6.23
18 Jan 2020	6.2	8.3	240	150	0.59	0.51	11.30	2.47
16 – 17 Dec 2020	7.2	8.3	180	180	0.62	0.54	13.00	-3.37
31 Jan – 1 Feb 2021	9.3	11.4	165	135	0.67	0.52	7.28	3.10
All cases	7.2	9.3	165	150	0.63	0.52	13.80	2.30

515 Table 3. Median duration, thickness, upward motion (Doppler velocity without estimated sedimentation), and  
 516 reflectivity from the KASPR VPT moments for UR with  $SW > 0.4 \text{ m s}^{-1}$  (URSWHI) and  $SW < 0.4 \text{ m s}^{-1}$   
 517 (URSWLO) found at heights  $> 1.2 \text{ km}$ .  
 518

519

520 *b. Relationships between the updraft regions and wind shear*

521 For the cases in this study, soundings and KASPR RHI measurements suggest a relationship  
 522 between vertical wind shear and SW. We investigate the relationship between UR and vertical  
 523 wind shear by examining moist Richardson number and frontogenesis. Figure 15 shows time stack  
 524 plots for vertical wind shear at 1–8 km altitudes based on VAD technique from KASPR PPI at an  
 525 elevation angle of  $15^\circ$  every 7 minutes. In Fig. 15, color-coded subsets along each bar indicate  
 526 wind shear characteristics with a threshold of  $20 \text{ m s}^{-1} \text{ km}^{-1}$ . This figure represents predominant  
 527 wind shear values with the threshold. The wind shear estimated from VAD are mean values at  
 528 each altitude in the PPI scan where the volume size of each layer is a function of height (7.5 km in  
 529 horizontal size at the height of 1 km).

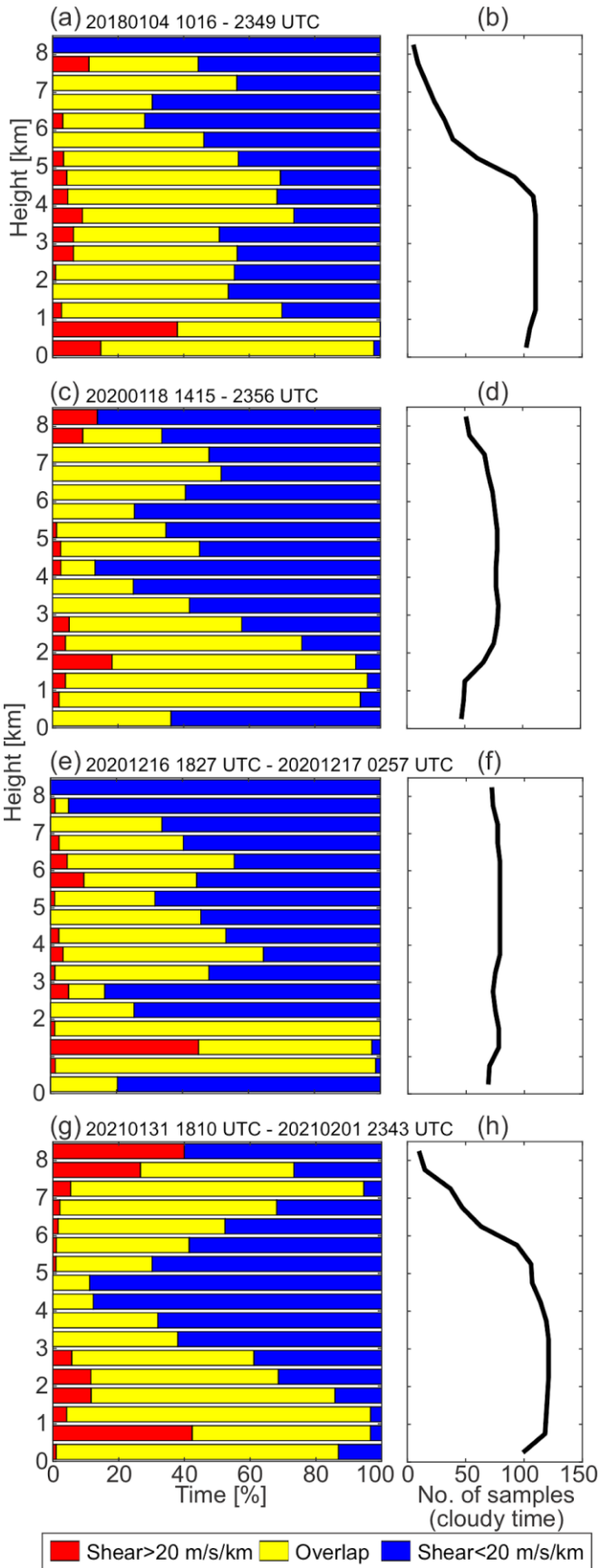
530 Generally, the peaks of the UR occurrence shown in Fig. 14 correspond to the peaks of larger  
531 wind shear occurrence (red + yellow bars), but there is case-to-case variability. The case of 4  
532 January shows three peaks of the updraft occurrence (1.5, 4.5, and 9 km altitudes), and URSWHI  
533 has large contributions to the 1.5 and 4.5 altitude peaks. These peaks coincide with the peak of  
534 larger wind shear (red and yellow bars in Fig. 15a) at ~1 and 3.5-5 km altitudes, where the stable  
535 with wind shear layers shown in the sounding are included (Fig. 5c).

536 Similar to the 4 January case, the cases of 16-17 December and 1 February also show a peak  
537 of the occurrence of the URSWLOs at 9-10 km. URSWHI has local maxima at lower altitude than  
538 that of URSWLOs (around 4.5 and 6.5 km for 16-17 December and around 3 and 7.5 km for 1  
539 February). Those local maxima in the URSWHI include a significant time (up to ~60% of cloudy  
540 time for 16-17 December and up to ~90% of cloudy time for 1 February) dominated by larger wind  
541 shear. These layers include at least wind shear layers observed in the soundings (Fig. 9c and 11c).

542 The single-band case on 18 January 2020, also has a peak of the URSWLO occurrence near  
543 the cloud top (9-10 km). This case produced only a few URSWHIs. For this case, larger wind shear  
544 was observed at any altitudes as it is observed in the other multi-band cases (Fig. 15b).

545 In summary, the common characteristic among the four cases is the peak of the URSWLO  
546 occurrence near the cloud tops. They are found above 8 km altitude; some of them are found very  
547 close to the echo tops, and most of them are found within 1-2 km distance from the echo tops. The  
548 lower SW is likely due to a combination of less turbulence and a narrower particle size distribution  
549 owing to weaker reflectivity. Since the VAD-based wind data are limited to 7.8 km maximum  
550 altitude, the relationship between these > 8 km altitude updrafts and wind shear is unclear in this  
551 study. There are a few common characteristics shown in the multi-band cases. First, the peak of  
552 the URSWHI occurrence is found at a lower altitude than that of the URSWLOs. Considering that  
553 the contribution of particle size distribution to SW could be  $SW < 0.2 \text{ m s}^{-1}$  (Appendix A), the  
554 large SW ( $> 0.4 \text{ m s}^{-1}$ ) could suggest a presence of small-scale turbulence in the radar range-gates.  
555 Second, the height of the higher occurrence of the URSWHI is dominated by larger wind shear ( $>$   
556  $20 \text{ m s}^{-1} \text{ km}^{-1}$ ). Although the wind shear itself could contribute to the total SW, wind shear could  
557 also work as a trigger of microscale updrafts. Comparisons between the altitudes where there is  
558 more frequent occurrence of high SW (Fig. 14) with where there is more frequent occurrence of  
559 wind shear (Fig. 15) do not closely correspond. These variabilities suggest a need for

560 considerations of time variations of wind shear layer, storm evolution such as frontogenesis, and  
561 shear instability (relationship with thermodynamic stability).



563 Figure 15: Histograms of occurrence (accumulated time relative to the total cloudy echo time observed by  
564 KASPR PPIs at an elevation angle of  $15^\circ$ ) at each height with different values of shear for storms on 4 Jan 2018,  
565 18 Jan 2020, 16 – 17 Dec 2020, and 31 Jan –1 Feb 2021. Wind shear estimated from the VAD technique using  
566 the KASPR PPI measurements. Wind shear threshold is  $20 \text{ m s}^{-1} \text{ km}^{-1}$ . The wind shear was estimated using slant-  
567 range 0.5-km windows ( $\sim 132 \text{ m}$  in height) within each 0.5 km layer. In a resampled 0.5 km height range, some  
568 of the samples with the wind shear  $> 20 \text{ m s}^{-1} \text{ km}^{-1}$  and  $< 20 \text{ m s}^{-1} \text{ km}^{-1}$  located at different height can be  
569 overlapped in time. Periods where wind shear  $> 20 \text{ m s}^{-1} \text{ km}^{-1}$  and wind shear  $< 20 \text{ m s}^{-1} \text{ km}^{-1}$  are overlapped in  
570 time are represented by yellow bars. The wind shear estimated from VAD is along the conical PPI scan whose  
571 radius increases with increasing height (7.5 km in horizontal size at the height of 1 km). As a result, the VAD  
572 samples a different volume from the VPT measurements.  
573

574 *c. Relationships between the updraft regions and storm evolution*

575 To investigate the spatial characteristics of URs associated with wind shear, we show locations  
576 of the detected updraft regions (dots) in the height-time cross section fields for individual cases in  
577 Figs. 16a – 19a, with color shade representing SW from the KASPR VPT measurements and  
578 grayscale representing KASPR reflectivity from VPT. We also show wind directions (color shade)  
579 and vertical wind shear (contours) from the KASPR VAD analysis in Figs. 16b – 19b.

580 In addition, we estimate the upward mass flux based on the detected URs, and moist  
581 Richardson Number (mRi, Eq. 2) using the KASPR VAD measurements. The mass flux (MF) at  
582 each altitude can be estimated as:

$$583 \quad MF = \bar{W} \rho_d UF \text{ [kg m}^{-2} \text{ s}^{-1}] \quad (3)$$

584 where  $\bar{W}$  is the mean updraft which is the positive Doppler velocity from the detected updraft  
585 regions averaged over time at each altitude,  $\rho_d$  is the dry air density estimated from the nearest-  
586 time sounding measurements, and  $UF$  is the updraft fraction estimated as the ratio of the time of  
587 updraft (positive Doppler velocity in the detected updraft regions) to the total cloudy time for each  
588 VPT file. The mass flux profile from each VPT file is then averaged over height  $> 1.2 \text{ km}$  for each  
589 VPT file. The height-time cross sections of mass flux and mean mass flux are displayed in the time  
590 series plots in Figs. 16c–18c and 16d–19d, respectively. Figures 16c–19c also show the mRi less  
591 than 0.25 using sounding and KASPR VAD data. Finally, to examine a relation with a large scale  
592 forcing, we also show the time series of frontogenesis at 600, 700, 775, and 800 hPa using RAP  
593 reanalysis data in Figs. 16e – 19e.  
594

595 For the 4 January case (Fig. 16), the earlier snowband period (1110–1800 UTC) is associated  
596 with 600-hPa frontogenesis, with a peak exceeding  $10 \text{ K (100 km)}^{-1} (3\text{hr})^{-1}$  (Fig. 16e, light blue),  
597 while there is 700-hpa frontogenesis exceeding  $15 \text{ K (100 km)}^{-1} (3\text{hr})^{-1}$  for the latter snowband

598 (1900 – 2110 UTC) (Fig. 16e, blue). A difference between the two snowband periods is that the  
599 first accompanied URSWHIs (Fig. 16a, represented by brown-red dots) producing relatively large  
600 mass flux at around 1600 UTC (Fig. 16c,  $\sim 0.08 \text{ kg m}^{-2} \text{ s}^{-1}$ ). The URSWHIs appear in the mid-level  
601 of the cloud, consistent with the earlier snowband period producing reflectivity  $>20 \text{ dBZ}$  below 4  
602 km altitude, which is 5-dB stronger than that of the latter snowband (Fig. 16a). The URSWHI  
603 height is 6 km at 1300 UTC and then descends to 3.5-4 km at 1800 UTC (Fig. 16a), while the  
604 URSWLO (represented by yellow-green dots) are found at 2-km below the cloud top before the  
605 snowband period from 1000 to 1300 UTC. From the KASPR VAD (Fig. 16b), this period (1300 -  
606 1800 UTC) when the height URSWHIs dominate the mid-levels corresponds to the easterly wind  
607 associated with the cyclone below 5 km (Fig. 5b). This low-level wind produces a vertical wind  
608 shear with the upper-level southerly wind shown in the sounding (Fig. 5c). The low-level easterly  
609 flow corresponds to the warm advection shown at 700 hPa. The URSWHIs are also collocated  
610 with vertical wind shear  $> 20 \text{ m s}^{-1} \text{ km}^{-1}$  in the KASPR VAD (Fig. 16b, black contour). This is  
611 consistent with the low  $m\text{Ri} < 0.25$  (Fig. 16d, contour), and the upward mass flux (Fig. 16c) occurs  
612 within and above it. The number of the URs decreases after 1830 UTC close to the end of the first  
613 snowband passage and the frontal passage. The latter snowband accompanied less URs producing  
614 smaller mass flux and smaller reflectivity. The low  $m\text{Ri}$  is still present at 4 km altitude, but the  
615 wind direction changes to north to northwesterly.

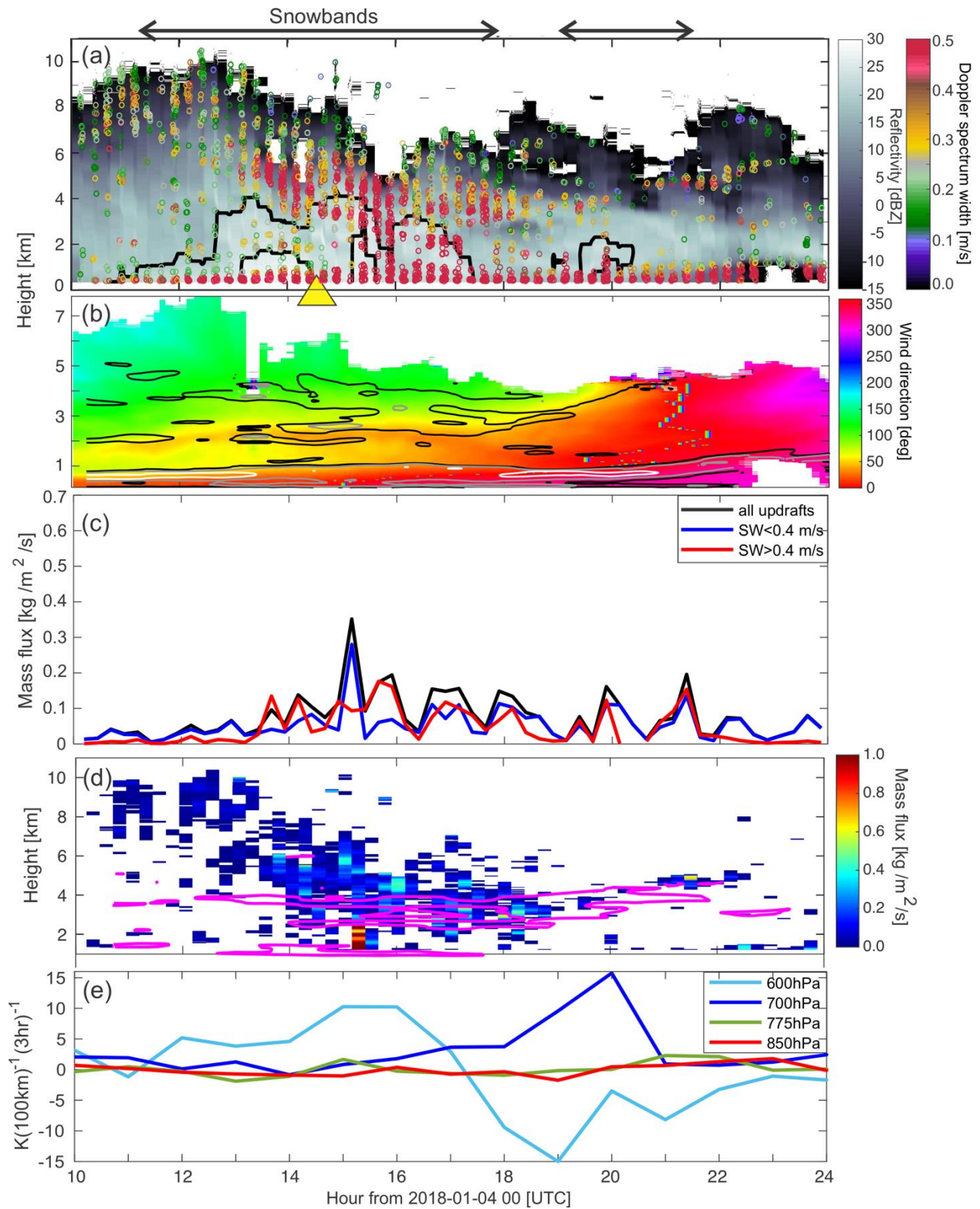
616 For the 16-17 December case (Fig. 18), the snowband period is also closely associated with  
617 the 600-hPa frontogenesis, with the peak exceeding  $15 \text{ K (100 km)}^{-1} (3\text{hr})^{-1}$  at 0200 UTC on 17  
618 December (Fig. 18e). URSWLOs are found within 2 km from the cloud top height starting before  
619 the snowband period from 1930 UTC 16 December to 0200 UTC 17 December (Fig. 18a).  
620 URSWHIs appear from 2100 UTC 16 December just below the URSWLO layer, corresponding  
621 to the period that includes larger reflectivity  $>25 \text{ dBZ}$  below 2 km (2230-0010 UTC) and below  
622 4.5 km (0030 - 0145 UTC, snowband period). During the snowband period, URSWHIs are more  
623 prominent in a deeper layer between 4 km to the cloud top. The URSWHIs contribute to large  
624 mass flux attaining  $\sim 0.4 \text{ kg m}^{-2} \text{ s}^{-1}$  at around 0115 UTC on 17 Dec. (Fig. 18c). The KASPR VAD  
625 analysis (Fig. 18b) shows that the lower boundary of the URSWHI layer well corresponds to  
626 vertical wind shear  $> 20 \text{ m s}^{-1} \text{ km}^{-1}$  (Fig. 18b) starting at 6.2 km altitude at 2100 UTC until 3-4 km  
627 at 0230 UTC and low  $m\text{Ri} < 10^{-2}$  (Fig. 18d, red contour). The upward mass flux is observed above  
628 the vertical wind shear and low  $m\text{Ri}$  layers (Fig. 18d).

629 For the 1 February case (Fig. 19), the snowband period is associated with a 700 hPa  
630 frontogenesis of  $7 \text{ K (100 km)}^{-1} (3\text{hr})^{-1}$  at 1800 UTC, and the 775 hPa frontogenesis maximum of  
631  $15 \text{ K (100 km)}^{-1} (3\text{hr})^{-1}$  at 2000 UTC (Fig. 19e). URSWLOs (represented by yellow-green dots)  
632 are observed near the cloud top with weak reflectivity ( $< \sim 0 \text{ dBZ}$ ) from the beginning of the  
633 observation on 31 Jan. (1800 UTC) until 1300 UTC on 1 February. URSWHI occurs from 1200  
634 UTC 1 February to the end of the analysis period (0000 UTC 2 February), which is consistent with  
635 the snowband period. The URSWHIs contribute to large mass flux exceeding  $0.15 \text{ kg m}^{-2} \text{ s}^{-1}$  with  
636 the maximum  $> 0.5 \text{ kg m}^{-2} \text{ s}^{-1}$  at 1800 UTC and reflectivity  $> 20 \text{ dBZ}$  below 4 km. The URSWHIs  
637 (Fig. 19a) and upward mass flux (Fig. 19d) are found above the layer of large vertical wind shear  
638  $> 30 \text{ m s}^{-1} \text{ km}^{-1}$  (Fig. 19b, gray contour) and low  $m\text{Ri} < 0.25$  (Fig. 19d, contour). The KASPR  
639 VAD analysis (Fig. 19b) shows the vertical wind shear produced by south-southeasterly wind in  
640 the low altitudes and southwesterly wind in the upper altitudes, similar to the 16-17 December  
641 case. The shear line is found between 2 and 3 km altitudes until 1210 UTC on 1 February and then  
642 ascends to 6 km altitude by 1400 UTC. The low-level south-southeasterly wind corresponds to the  
643 700 hPa warm advection.

644 In contrast to these three multi-band cases, the 18 January case is associated with very weak  
645 frontogenesis at all levels around Long Island ( $< 2 \text{ K (100 km)}^{-1} (3\text{hr})^{-1}$ , Fig. 17e) and near-zero  
646 mass flux (Fig. 17c, less than  $0.05 \text{ kg m}^{-2} \text{ s}^{-1}$  except 2220 UTC). The snowband closely corresponds  
647 to the weak frontogenesis peaks ( $\sim 2 \text{ K (100 km)}^{-1} (3\text{hr})^{-1}$ ) at 700, 775, and 800 hPa. Similar to the  
648 other three cases, URSWLOs (represented by yellow-green-blue dots) are observed near the cloud  
649 top with weak reflectivity ( $< \sim 0 \text{ dBZ}$ ). There is no clear correlation between the URSWHI and  
650 snowband. Shallow regions with vertical wind shear  $> 30 \text{ m s}^{-1} \text{ km}^{-1}$  (Fig. 17b) are observed within  
651 the cloud, similar to the other three cases.

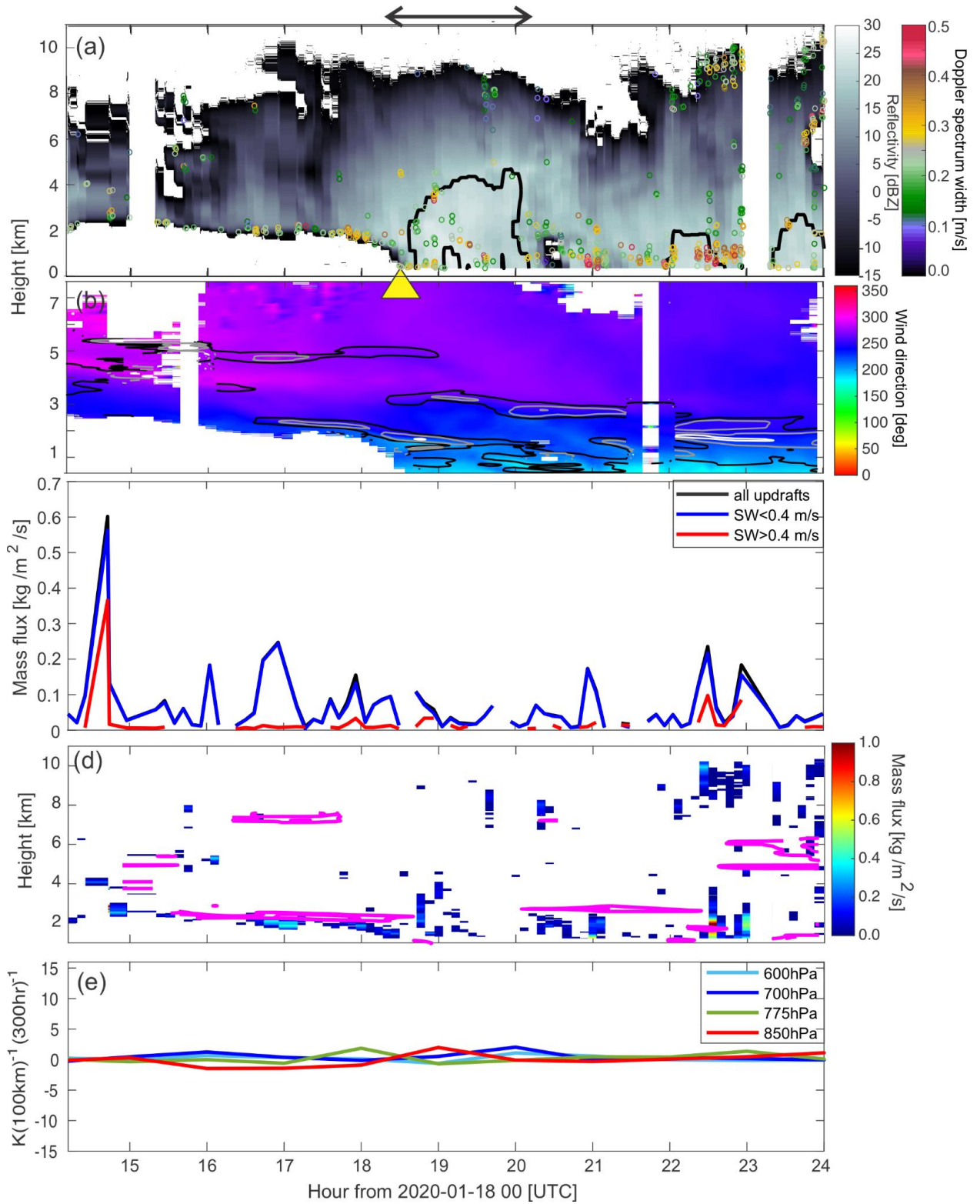
652 The URs are found throughout the snowstorms regardless of the snowband periods or  
653 frontogenesis for the four cases. The URSWHIs are well correlated with the snowbands for three  
654 of the cases. The URSWHI clusters during the snowband periods and the upward mass flux are  
655 generally found just above the vertical wind shear ( $> 20 \text{ m s}^{-1} \text{ km}^{-1}$ ) layer and the low  $m\text{Ri} (< 0.25)$   
656 layer, suggesting a role of shear instability for generating URs and hence upward mass transports.  
657 The URs contribute to positive mass flux when the URs updrafts tend to cluster near each other in  
658 space and time, suggesting that the URs can play a role in forming/growing precipitation particles.  
659 Near the cloud top, where URSWLOs dominate, the mass flux varies in magnitude and is

660 discontinuous in time. RAP 700 hPa specific humidity  $> 5 \text{ g kg}^{-1}$  (not shown) is associated with  
 661 periods with larger mass flux in all four cases.



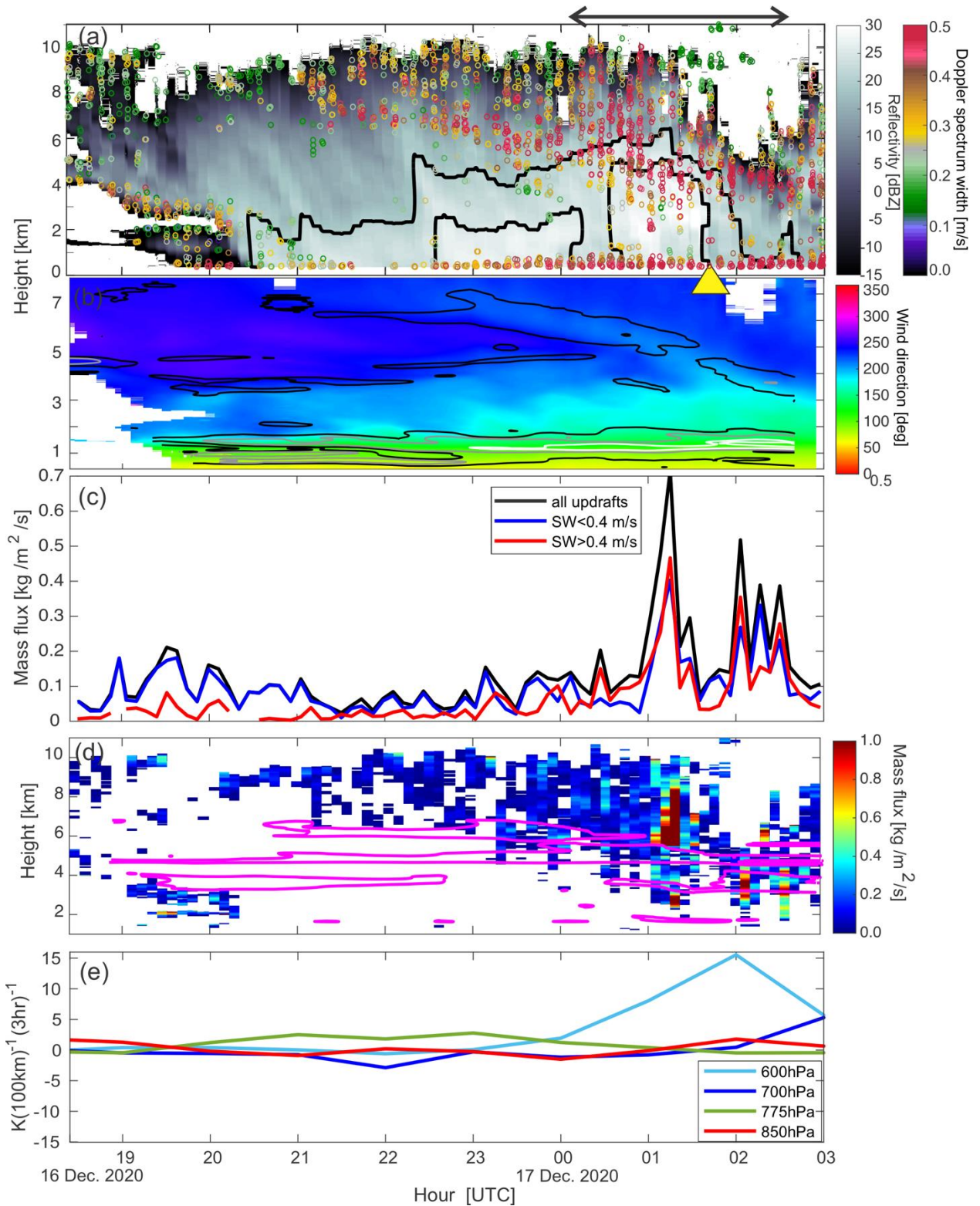
662

663 Figure 16: Time series of (a) KASPR reflectivity from VPT (gray scale) and locations of  
664 detected updraft regions (color dots), black contours represent KASPR reflectivity >20 dBZ  
665 with 5 dB increment.(b) wind direction (color shade) and vertical wind shear of 0.02, 0.03, and  
666 0.05 s<sup>-1</sup> (black, gray, and white contours, respectively) estimated from KASPR VAD, (c) mass  
667 flux estimated from the detected updraft regions averaged over altitude, (d) height-versus-time  
668 cross sections of the mass flux (color shade) and moist Richardson Number smaller than 10<sup>-0.6</sup>  
669 (magenta contour), and (e) frontogenesis at four levels estimated using RAP reanalysis data  
670 for 4 Jan., 2018. The mass flux is averaged every VPT file for (c) and (d) and then averaged  
671 over altitude for (c). Black line in (c) represents the mass flux from the contributions of all  
672 detected updraft regions, and blue and red lines represent that of updraft regions with SW>0.4  
673 m s<sup>-1</sup> and <0.4 m s<sup>-1</sup>, respectively. The zoom-up of the rectangle region is also displayed in (c).  
674 Horizontal arrows on the top of (a) represent the period of snowband passages at SBU. Yellow  
675 triangle in (a) indicates the time of RHI measurements shown in Fig. 6.  
676



677  
678  
679

Figure 17: Same as Fig. 16, but for 18 Jan 2020.



680  
681

Figure 18: Same as Fig. 16, but for 16 – 17 Dec 2020.

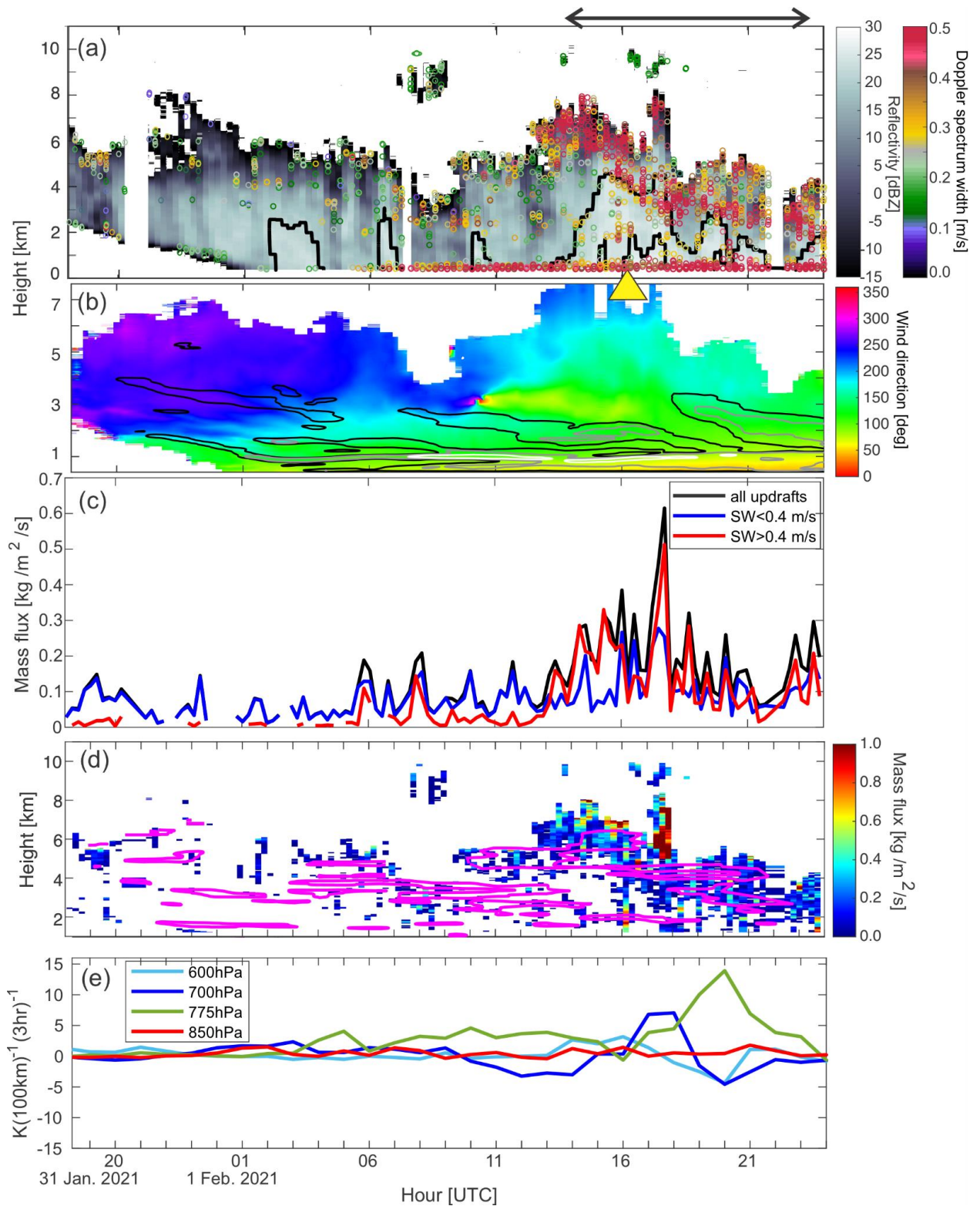


Figure 19: Same as Fig. 16, but for 31 Jan– 1 Feb 2020.

682  
683  
684  
685

## 686 5. Summary

687 We investigated the relations among microscale updraft regions (URs) and snowbands, vertical  
688 wind shear, stability, frontogenesis, and upward mass transport for four winter snowstorm cases  
689 (4 January 2018; 18 January 2020; 16-17 December 2020; 1 February 2021). Measurements were  
690 made as each storm passed over the Stony Brook and Brookhaven National Laboratory Radar  
691 Observatory (SBRO) in Stony Brook, NY and included periods with and without snowbands and  
692 in the northwest and northeast quadrants of the three storms (4 January, 16 – 17 December, and 1  
693 February) and the southwest quadrant of the 18 January storm. The three of the cases (4 January,  
694 16 – 17 December, and 1 February) included more than one snowband.

695 The mean Doppler velocity from the vertically-pointing Ka-band polarimetric radar  
696 measurements was used to identify updraft regions in this study. After the removal of hydrometeor  
697 sedimentation from the VPT measured mean Doppler velocity, the updraft region was simply  
698 defined as a region with the estimated vertical air motion (VPT measured mean Doppler velocity  
699 minus estimated particle fall speed) greater than or equal to  $0.4 \text{ m s}^{-1}$  (negative sign of Doppler  
700 velocity indicates a downward motion). Using vertically-pointing radar data does not provide  
701 information on the lifecycle of the updrafts, but the duration of the updraft overhead can be  
702 converted to an estimated spatial scale using horizontal wind estimated from a KASPR PPI VAD  
703 technique. We estimated mass flux based on the detected updraft regions and sounding data and  
704 investigated relationships among updraft regions, mass flux, and frontogenesis, and shear  
705 instability to discuss roles of mesoscale instability on generating the updrafts and vertical mass  
706 transport. We summarize the characteristics of the updraft regions and their associations with  
707 spectral width, wind shear and frontogenesis:

- 708 ● In the vertical pointing radar data, the distribution of updraft durations is approximately  
709 logarithmic with most individual updrafts passing overhead in only a few seconds (<20  
710 sec) (Fig. 13a). They are roughly equivalent to spatial scales < 500 m. The aspect ratio  
711 of the updraft regions estimated from the duration and horizontal scale has a lognormal  
712 frequency distribution with a modal value near 1 (Fig. 13b).
- 713 ● Overall, the snowbands occur in a region of low to mid-level frontogenesis, but the  
714 microscale updraft regions are found at all altitudes, occur both in regions with and  
715 without snowbands, and do not appear to be closely associated with frontogenesis (Fig.  
716 16-19).

- 717 • The subset of updraft regions with larger VPT Doppler spectrum width ( $SW > 0.4 \text{ m s}^{-1}$ )  
718  $^1$ ), which imply more turbulent updrafts, frequently occur within mid-levels of the  
719 storms (several km below cloud echo top). Updrafts with smaller  $SW (< 0.4 \text{ m s}^{-1})$   
720 occur from near surface to near cloud tops (Fig. 14)
- 721 • Updraft regions that tend to be closer together in space and time yield more vertically-  
722 integrated mass flux. The duration of individual updraft regions is not the primary  
723 factor of the mass flux (Fig. 16-19).
- 724 • The highest mass flux is produced roughly coincident in time and slightly above shear  
725 instability layers during the snowband periods, suggesting that the updraft regions can  
726 be triggered in the shear unstable layers (Fig. 16-19).

727 The analysis illustrates that microscale updrafts can contribute to the precipitation mass growth  
728 regardless of whether snowbands are present or not. Future studies should examine the relative  
729 roles of microscale updrafts as compared to mesoscale and synoptic scale updrafts to better  
730 understand the precipitation production in winter storms, which in turn may aid in reducing  
731 uncertainties in snowfall accumulation forecasts. The methodology to identify microscale updrafts  
732 described in this paper can be applied to other vertically-pointing Doppler radar datasets to  
733 examine the small scale velocity structures that are too fine scale to be resolved by other sensors  
734 such as the US National Weather Service PPI scanning radars. Further analysis of microscale  
735 updrafts can also shed light on the degree to which ice precipitation mass changes in a more  
736 episodic mode (smaller time and space scales) versus a more continuous mode (longer time and  
737 scale scales) in winter storms and in stratiform regions. We detected many microscale updrafts in  
738 the boundary layer ( $< 1.2 \text{ km}$  altitude) during portions of each of the four storms but did not focus  
739 on them in this study. These low-level updrafts may further modify the microphysics and would  
740 be an interesting topic for future studies.

741

742

## 743 **Appendix A**

744 There are six major Doppler spectral broadening mechanisms that contribute to the measured  
745 spectrum width  $\sigma_{tot}$  (Doviak and Zrnić, 2006): different hydrometeor particle terminal velocity of  
746 different sizes  $\sigma_{psd}$ , turbulence  $\sigma_{tur}$ , mean horizontal wind shear  $\sigma_{shr}$ , cross wind  $\sigma_{crs}$ , antenna

747 motion  $\sigma_{ant}$ , and variation of orientation and vibrations of hydrometeor  $\sigma_{ori}$ . Those contributions  
 748 can be written as:

$$749 \quad \sigma_{tot} = \sqrt{\sigma_{psd}^2 + \sigma_{tur}^2 + \sigma_{shr}^2 + \sigma_{crs}^2 + \sigma_{ant}^2 + \sigma_{ori}^2} \quad (A1)$$

750 To simplify, the contributions of  $\sigma_{ant}$  and  $\sigma_{ori}$  are ignored, assuming that they are negligible  
 751 compared to the other terms. Moreover, for the VPT measurements,  $\sigma_{shr}$  and  $\sigma_{crs}$  can also be  
 752 negligible compared to  $\sigma_{psd}$  and  $\sigma_{tur}$ . For the VPT measurements in this study, we consider the  
 753  $\sigma_{psd}$  and  $\sigma_{tur}$  to evaluate the contributions to  $\sigma_{tot}$  as:

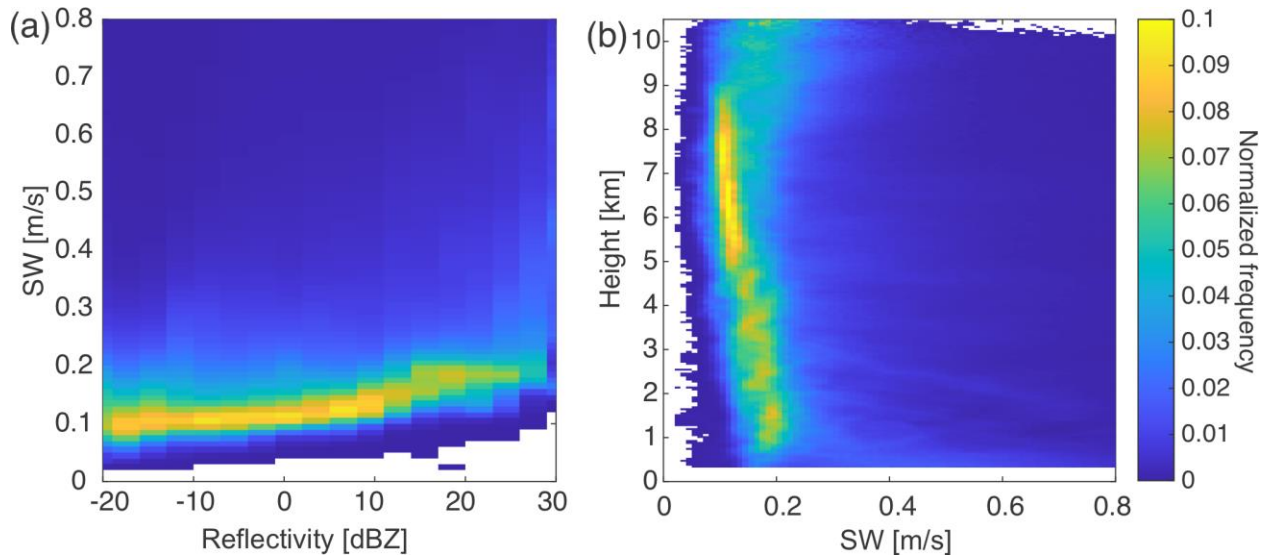
$$754 \quad \sigma_{tot} = \sqrt{\sigma_{psd}^2 + \sigma_{tur}^2} \quad (A2)$$

755 To estimate general  $\sigma_{psd}$  for the present cases, Fig. A1a shows a frequency distribution of SW  
 756 versus reflectivity from the KASPR VPT measurements collected during the selected four events  
 757 in this study. In this figure, we assume that  $\sigma_{psd}$  can be correlated with reflectivity statistically.  
 758 The SW with the maximum frequency at each reflectivity bin increased with reflectivity. This can  
 759 represent statistical  $\sigma_{psd}$  associated with reflectivity. The SW with maximum frequency is  
 760 generally less than  $0.2 \text{ m s}^{-1}$ . For the four cases, which are stratiform snow events, radar reflectivity  
 761 generally increases with decreasing height, suggesting that hydrometeor particles generally grow  
 762 downward. As the particle size distribution broadens with increasing reflectivity,  $\sigma_{psd}$  which is  
 763 attributed to the spread of particle fall speeds in the radar resolution volume can also increase.  
 764 Figure A1b shows vertical frequency distribution of the SW. The SW with maximum frequency  
 765 increases downward and is generally less than  $0.2 \text{ m s}^{-1}$ .

766 Figure A2 shows the relationship of Eq. A2 to represent the contributions of  $\sigma_{psd}$  and  $\sigma_{tur}$  to  
 767  $\sigma_{tot}$ . At  $\sigma_{tot}$  (observed SW) =  $0.3 \text{ m s}^{-1}$  with  $\sigma_{psd} = 0.2 \text{ m s}^{-1}$ ,  $\sigma_{tur}$  is approximately  $0.2 \text{ m s}^{-1}$ ,  
 768 comparable with  $\sigma_{psd}$ . For  $\sigma_{tot} > 0.35 \text{ m s}^{-1}$  with  $\sigma_{psd} = 0.2 \text{ m s}^{-1}$ ,  $\sigma_{tur} > \sigma_{psd}$ , indicating that  $\sigma_{tur}$   
 769 can be a primary contribution to the observed SW. We use  $\sigma_{tot} = 0.4 \text{ m s}^{-1}$  for the threshold of  
 770 observed SW to classify detected updraft regions related to turbulence. When we compared  
 771 statistics using a threshold of  $\sigma_{tot} = 0.4 \text{ m s}^{-1}$  and a threshold of  $0.5 \text{ m s}^{-1}$ , the medians of duration  
 772 and depth for URSWHI and URSWLO did not change much (less than 1 sec and less than 15 m,  
 773 respectively). The medians of reflectivity and upward motion slightly increased as we expected;  
 774 median reflectivity for URSWHI increased by  $\sim 0.5 \text{ dB}$  and that for URSWLO increased by  $\sim 2 \text{ dB}$ ,  
 775 and median upward motions for both URSWHI and URSWLO increased by less than  $0.05 \text{ m s}^{-1}$ .

776

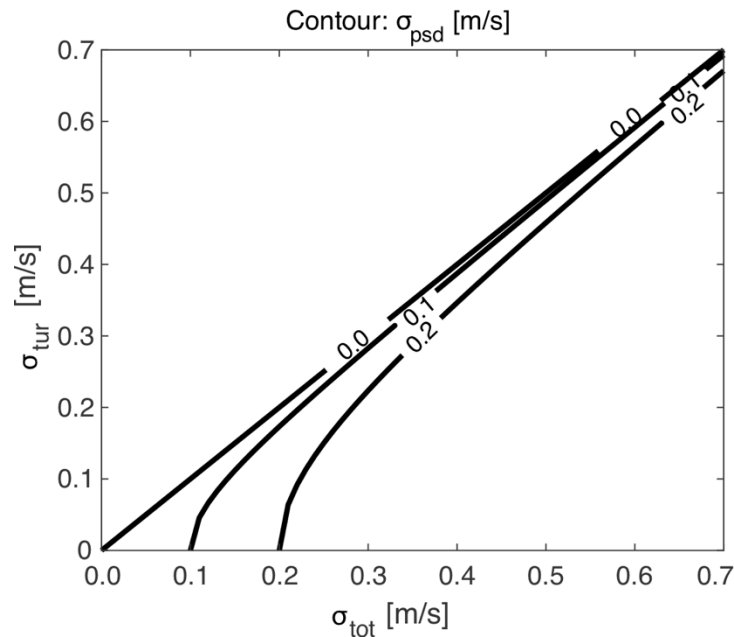
777



778

779 Figure A1: (a) Frequency distribution of SW versus reflectivity from the KASPR VPT  
780 measurements collected during the four events. Color shade represents the frequency normalized  
781 every 2 dBZ from -20 dBZ. (a) Frequency by altitude distribution of SW. Color shade represents  
782 the frequency normalized at each radar range-gate (every 15 m).

783



784

785 Figure A2:  $\sigma_{tur}$  versus  $\sigma_{tot}$  diagram with corresponding  $\sigma_{psd}$  based on Eq. A2.

786

787

788

789 *Acknowledgments.*

790 This work was supported by the National Science Foundation (Yuter: AGS-1347491 and AGS-  
791 1905736; Colle: AGS-1904809; Oue and Kollias: AGS-1841215) and the National Aeronautics  
792 and Space Administration (Yuter: 80NSSC19K0354).

793

794 *Data Availability Statement.*

795 KASPR and sounding data used in this study are available at Stony Brook University Academic  
796 Commons Repository (<https://commons.library.stonybrook.edu/somasdata/17>). Those data collected  
797 under IMPACTS are also available at the NASA Global Hydrometeorology Resource Center (GHRC)  
798 DAAC system (<http://dx.doi.org/10.5067/IMPACTS/RADAR/DATA101>,  
799 <http://dx.doi.org/10.5067/IMPACTS/SOUNDING/DATA301>).

800

801

802 **References**

- 803 Benjamin, S. G., S. S. Weygandt, J. M. Brown, M. Hu, C. R. Alexander, T. G. Smirnova, J. B. Olson, E. P.  
804 James, D. C. Dowell, G. A. Grell, H. Lin, S. E. Peckham, T. L. Smith, W. R. Moninger, J. S. Kenyon,  
805 and G. S. Manikin, 2016: A North American Hourly Assimilation and Model Forecast Cycle: The Rapid  
806 Refresh. *Monthly Weather Review* 144, 4, 1669-1694, <https://doi.org/10.1175/MWR-D-15-0242.1>
- 807 Bosart, L. F., and F. Sanders, 1986: Mesoscale Structure in the Megalopolitan Snowstorm of 11–12  
808 February 1983. Part III: A Large-Amplitude Gravity Wave. *J. Atmos. Sci.*, 43, 924– 939,  
809 [https://doi.org/10.1175/1520-0469\(1986\)043<0924:MSITMS>2.0.CO;2](https://doi.org/10.1175/1520-0469(1986)043<0924:MSITMS>2.0.CO;2).
- 810 Browning, K. A., and R. Wexler, 1968: The determination of kinematic properties of a wind field using  
811 Doppler radar. *J. Appl. Meteorol.*, 7, 105–113, doi: 10.1175/1520-  
812 0450(1968)007<0105:TDOKPO>2.0.CO;2.
- 813 Colle, B. A., D. Stark, and S. E. Yuter, 2014: Surface microphysical observations within East Coast winter  
814 storms on Long Island, New York. *Mon. Wea. Rev.*, 142, 3126–3146, doi:10.1175/MWR-D-14-  
815 00035.1.
- 816 Doviak, R. J., and D. S. Zrnic (2006): Doppler radar and weather observations, 2nd ed., San Diego,  
817 Academic Press, Second Addition.
- 818 Ganetis, S. A., B. A., Colle, S. E. Yuter, and N. P. Hoban, 2018: Environmental Conditions Associated with  
819 Observed Snowband Structures within Northeast U.S. Winter Storms, *Monthly Weather Review* Vol.  
820 146, No. 11, pp 3675, 1520-0493
- 821 Jurewicz, M. L., Sr., and M. S. Evans, 2004: A comparison of two banded, heavy snowstorms with very  
822 different synoptic settings. *Wea. Forecasting*, 19, 1011-1028, <https://doi.org/10.1175/WAF-823.1>.
- 823 Keeler, J. M., B. F. Jewett, R. M. Rauber, G. M. McFarquhar, R. M. Rasmussen, L. Xue, C. Liu, and G.  
824 Thompson, 2016a: Dynamics of cloud-top generating cells in winter cyclones. Part I: Idealized  
825 simulations in the context of field observations. *J. Atmos. Sci.*, 73, 1507–1527,  
826 <https://doi.org/10.1175/JAS-D-15-0126.1>.
- 827 Keeler, J. M., B. F. Jewett, R. M. Rauber, G. M. McFarquhar, R. M. Rasmussen, L. Xue, C. Liu, and G.  
828 Thompson, 2016b: Dynamics of cloud-top generating cells in winter cyclones. Part II: Radiative and  
829 instability forcing. *J. Atmos. Sci.*, 73, 1529–1553, <https://doi.org/10.1175/JAS-D-15-0127.1>.
- 830 Keeler, J. M., B. F. Jewett, R. M. Rauber, G. M. McFarquhar, R. M. Rasmussen, L. Xue, C. Liu, and G.  
831 Thompson, 2017: Dynamics of cloud-top generating cells in winter cyclones. Part III: Shear and  
832 convective organization. *J. Atmos. Sci.*, 74, 2879-2897, <https://doi.org/10.1175/JAS-D-16-0314.1>.
- 833 Kollias, P., N. Bharadwaj, K. Widener, I. Jo, and K. Johnson, 2014: Scanning ARM cloud radars. Part I:  
834 Operational sampling strategies. *Journal of Atmospheric and Oceanic Technology*, 31(3), 569– 582

835 Kollias, P., E. Luke, M. Oue, and K. Lamer, 2020: Agile adaptive radar sampling of fast-evolving  
836 atmospheric phenomena guided by satellite imagery and surface cameras. *Geophysical Research Letters*,  
837 45, e2020GL088440. <https://doi.org/10.1029/2020GL088440>

838 Kumjian, M. R., and K. A. Lombardo, 2017: Insights into the Evolving Microphysical and Kinematic  
839 Structure of Northeastern U.S. Winter Storms from Dual-Polarization Doppler Radar, *Monthly Weather*  
840 *Review*, 145(3), 1033-1061.

841 Kumjian, M. R., S. A. Rutledge, R. M. Rasmussen, P. C. Kennedy, and M. Dixon, 2014: High-resolution  
842 polarimetric radar observations of snow-generating cells. *J. Appl. Meteor. Climatol.*, 53, 1636-1658,  
843 <https://doi.org/10.1175/JAMC-D-13-0312.1>.

844 Kumjian, M. R., D. M. Tobin, M. Oue, and P. Kollias, 2020: Microphysical Insights into Ice Pellet  
845 Formation Revealed by Fully Polarimetric Ka-band Doppler Radar. *J. Appl. Meteor. Climatol.*, doi:  
846 <https://doi.org/10.1175/JAMC-D-20-0054.1>

847 Lackmann, G. M., and G. Thompson, 2019: Hydrometeor Lofting and Mesoscale Snowbands. *Mon. Wea.*  
848 *Rev.*, 147, 3879-3899, <https://doi.org/10.1175/MWR-D-19-0036.1>.

849 Lamer, K., M. Oue, A. Battaglia, R. J. Roy, K. B. Cooper, R. Dhillon, and P. Kollias, 2021: Multifrequency  
850 radar observations of clouds and precipitation including the G-band, *Atmos. Meas. Tech.*, 14, 3615–  
851 3629, <https://doi.org/10.5194/amt-14-3615-2021>.

852 Markowski, P. M., and Y. P. Richardson, 2010: *Mesoscale Meteorology in Midlatitudes*. Wiley-Blackwell,  
853 424 pp.

854 McMurdie, L. A., G. M. Heymsfield, J. E. Yorks, S. A. Braun, G. Skofronick-Jackson, R. M. Rauber, S.  
855 Yuter, B. Colle, G. M. McFarquhar, M. Poellot, D. R. Novak, T. J. Lang, R. Kroodsma, M. McLinden,  
856 M. Oue, P. Kollias, M. R. Kumjian, S. J. Greybush, A. J. Heymsfield, J. A. Finlon, V. L. McDonald,  
857 and S. Nicholls, 2022: Chasing Snowstorms: The Investigation of Microphysics and Precipitation for  
858 Atlantic Coast-Threatening Snowstorms (IMPACTS) Campaign, *Bulletin of the American*  
859 *Meteorological Society*, 103, pp E1248, 1520-0477.

860 Molthan, A. L., B. A. Colle, S. E. Yuter, and D. Stark, 2016: Comparisons of Modeled and Observed  
861 Reflectivities and Fall Speeds for Snowfall of Varied Riming Degrees during Winter Storms on Long  
862 Island, New York, *Monthly Weather Review* Vol. 144, No. 11, pp 4327, 1520-0493

863 Morales, R. F., Jr., 2008: The historic Christmas 2004 south Texas snow event: Diagnosis of the heavy  
864 snow band. *Natl. Wea. Dig.*, 32, 135–152,  
865 <http://nwafiles.nwas.org/digest/papers/2008/Vol32No2/Pg135-Morales.pdf>.

866 Naeger, A. R., B. A. Colle, and A. Molthan, 2017: Evaluation of Cloud Microphysical Schemes for a Warm  
867 Frontal Snowband during the GPM Cold Season Precipitation Experiment (GCPEX). *Mon. Wea. Rev.*,  
868 145, 4627–4650, <https://doi.org/10.1175/MWR-D-17-0081.1>.

869 Naeger, Aaron R., B. A. Colle, N. Zhou, and A. Molthan, 2020: Evaluating Warm and Cold Rain Processes  
870 in Cloud Microphysical Schemes Using OLYMPEX Field Measurements, *Monthly Weather Review*  
871 Vol. 148, No. 5, pp 2163, 1520-0493

872 Novak, D. R., L. F. Bosart, D. Keyser, and J. S. Waldstreicher, 2004: An observational study of cold season-  
873 banded precipitation in Northeast U.S. cyclones. *Wea. Forecasting*, 19, 993-1010,  
874 <https://doi.org/10.1175/815.1>.

875 Novak, D. R., B. A. Colle, and A. Aiyyer, 2010: Evolution of mesoscale precipitation band environments  
876 within the comma head of northeast U.S. cyclones. *Mon. Wea. Rev.*, 138, 2354–2374.

877 Novak, D. R., B. A. Colle, and S. E. Yuter, 2008: High-Resolution Observations and Model Simulations of  
878 the Life Cycle of an Intense Mesoscale Snowband over the Northeastern United States. *Mon. Wea. Rev.*,  
879 136, 1433–1456, <https://doi.org/10.1175/2007MWR2233.1>.

880 Oue, M., P. Kollias, E. P. Luke, A. Ryzhkov, 2017: A New Ka-Band Scanning Radar Facility: Polarimetric  
881 and Doppler Spectra Measurements of Snow Events. AGU Fall Meeting, A31G-2270, New Orleans 11-  
882 15 December, 2017.

883 Oue, M., Kollias, P., Matrosov, S. Y., Battaglia, A., and Ryzhkov, A. V., 2021: Analysis of the  
884 microphysical properties of snowfall using scanning polarimetric and vertically pointing multi-  
885 frequency Doppler radars, *Atmos. Meas. Tech.*, 14, 4893–4913, [https://doi.org/10.5194/amt-14-4893-](https://doi.org/10.5194/amt-14-4893-2021)  
886 2021.

887 Petterssen, S., 1956: *Motion and Motion Systems*. Vol. 1, *Weather Analysis and Forecasting*, 2nd ed.,  
888 McGraw Hill, 428 pp.

889 Plummer, D. M., G. M. McFarquhar, R. M. Rauber, B. F. Jewett, and D. Leon, 2014: Structure and  
890 statistical analysis of the microphysical properties of generating cells in the comma-head region of  
891 continental winter cyclones. *J. Atmos. Sci.*, 71, 4181-4203, <https://doi.org/10.1175/JAS-D-14-0100.1>.

892 Plummer, D. M., G. M. McFarquhar, R. M. Rauber, B. F. Jewett, and D. C. Leon, 2015: Microphysical  
893 properties of convectively generated fall streaks within the stratiform comma head region of continental  
894 winter cyclones. *J. Atmos. Sci.*, 72, 2465–2483, <https://doi.org/10.1175/JAS-D-14-0354.1>.

895 Protat, A., and C. R. Williams, 2011: The Accuracy of Radar Estimates of Ice Terminal Fall Speed from  
896 Vertically Pointing Doppler Radar Measurements. *Journal of Applied Meteorology and Climatology*,  
897 50(10), 2120–2138.

898 Rauber, R. M., J. Wegman, D. M. Plummer, A. A. Rosenow, M. Peterson, G. M. McFarquhar, B. F. Jewett,  
899 D. Leon, P. S. Market, K. R. Knupp, J. M. Keeler, and S. M. Battaglia, 2014: Stability and charging  
900 characteristics of the commahead region of continental winter cyclones. *J. Atmos. Sci.*, 71, 1559-1582,  
901 <https://doi.org/10.1175/JAS-D-13-0253.1>.

902 Rauber, R. M., S. M. Ellis, J. Vivekanandan, J. Stith, W-C Lee, G. M. McFarquhar, and B. F. Jewett, 2017:  
903 Finescale structure of a snowstorm over the Northeastern United States: a first look at high resolution  
904 HIAPER Cloud Radar Observations. *Bull. Amer. Meteor. Soc.*, 98, 253-269,  
905 <https://doi.org/10.1175/BAMS-D-15-00180.1>.

906 Reges, H. W., N. Doesken, J. Turner, N. Newman, A. Bergantino, and Z. Schwalbe, 2016: CoCoRaHS:  
907 The evolution and accomplishments of a volunteer rain gauge network. *Bull. Amer. Meteor. Soc.*, 97,  
908 1831–1846, <https://doi.org/10.1175/BAMS-D-14-00213.1>.

909 Rosenow, A. A., D. M. Plummer, R. M. Rauber, G. M. McFarquhar, B. F. Jewett, and D. Leon, 2014:  
910 Vertical Velocity and Physical Structure of Generating Cells and Convection in the Comma Head  
911 Region of Continental Winter Cyclones. *J. Atmos. Sci.*, 71, 1538–1558. [https://doi.org/10.1175/JAS-D-](https://doi.org/10.1175/JAS-D-13-0249.1)  
912 [13-0249.1](https://doi.org/10.1175/JAS-D-13-0249.1).

913 Rosenow, A.A., R.M. Rauber, G.M. McFarquhar and J.M. Keeler, 2018: Elevated potential instability in  
914 the comma-head: Distribution and development. *Mon. Wea. Rev.*, 146, 1259-1278.  
915 <https://doi.org/10.1175/MWR-D-17-0283.1>.

916 Schultz, D. M., and J. A. Knox, 2007: Banded Convection Caused by Frontogenesis in a Conditionally,  
917 Symmetrically, and Inertially Unstable Environment, *Mon. Wea. Rev.*, 135(6), 2095-2110,  
918 <https://doi.org/10.1175/MWR3400.1>.

919 Schultz, D. M., and P. N. Schumacher, 1999: The Use and Misuse of Conditional Symmetric Instability,  
920 *Mon. Wea. Rev.*, 127, 2709-2732, [https://doi.org/10.1175/1520-](https://doi.org/10.1175/1520-0493(1999)127<2709:TUAMOC>2.0.CO;2)  
921 [0493\(1999\)127<2709:TUAMOC>2.0.CO;2](https://doi.org/10.1175/1520-0493(1999)127<2709:TUAMOC>2.0.CO;2).

922 Stark, D., B. A. Colle, and S. E. Yuter, 2013: Observed microphysical evolution for two East Coast winter  
923 storms and the associated snow bands. *Mon. Wea. Rev.*, 141, 2037–2057, doi:10.1175/MWR-D-12-  
924 00276.1.

925 Trapp, J. R., D. M. Schultz, A. V. Ryzhkov, and R. L. Holle, 2001: Multiscale structure and evolution of  
926 an Oklahoma winter precipitation event. *Mon. Wea. Rev.*, 129, 486–501, [https://doi.org/10.1175/1520-](https://doi.org/10.1175/1520-0493(2001)129<0486:MSAEOA>2.0.CO;2)  
927 [0493\(2001\)129<0486:MSAEOA>2.0.CO;2](https://doi.org/10.1175/1520-0493(2001)129<0486:MSAEOA>2.0.CO;2).

928 Xu, Q., 1992: Formation and evolution of frontal rainbands and geostrophic potential vorticity anomalies.  
929 *J. Atmos. Sci.*, 49, 629–648.

930 Zhang, F., S. E. Koch, C. A. Davis, and M. L. Kaplan, 2001: Wavelet analysis and the governing dynamics  
931 of a large-amplitude gravity wave event along the East Coast of the United States. *Quart. J. Roy. Meteor.*  
932 *Soc.*, 127, 2209–2245.

933 Zhang, F., C. Synder, and R. Rotunno, 2003: Effects of moist convection on mesoscale predictability. *J.*  
934 *Atmos. Sci.*, 60, 1173–1185.

935